Comparative analysis of three-column and three-column with central column semi-submersible platforms for floating wind turbines

Zou, Pengxu; Bricker, Jeremy D.

DOI
10.1016/j.oceaneng.2025.121615

Publication date
2025

Document Version
Final published version

Published in
Ocean Engineering

Citation (APA)
Zou, P., & Bricker, J. D. (2025). Comparative analysis of three-column and three-column with central column semi-submersible platforms for floating wind turbines. *Ocean Engineering*, *334*, Article 121615. https://doi.org/10.1016/j.oceaneng.2025.121615

Ocean Engineering 334 (2025) 121615

Contents lists available at ScienceDirect

Ocean Engineering

journal homepage: www.elsevier.com/locate/oceaneng

Research paper

Comparative analysis of three-column and three-column with central column semi-submersible platforms for floating wind turbines

Pengxu Zou [a,*], Jeremy D. Bricker [b,c]

[a] CCCC Guangdong-Hongkong-Macao Greater Bay Area Innovation Research Institute, Zhuhai, Guangdong, 519080, China
[b] Dept. of Civil and Environmental Engineering, University of Michigan, Ann Arbor, MI, 48109, USA
[c] Dept. of Hydraulic Engineering, Faculty of Civil Engineering & Geosciences, Delft University of Technology, 2600GA, Delft, the Netherlands

ARTICLE INFO

Keywords:
Floating wind turbine
Mooring response
Platform stability
Semi-submersible

ABSTRACT

Floating offshore wind turbines (FOWTs) are gaining increasing attention as a promising solution for harnessing wind energy in deep-water regions, where traditional bottom-fixed turbines are not feasible. Among the various floating platform designs, semi-submersible platforms have emerged as a leading candidate due to their balance of stability, adaptability, and cost-effectiveness. This paper presents a detailed comparative analysis of two typical types of semi-submersible platforms: the three-column design and the three-column with central column design. The study employs a coupled aero-hydro-mooring simulation system using OpenFOAM to evaluate the hydrodynamic, aerodynamic, and mooring dynamics of both platform configurations. High-fidelity computational fluid dynamics (CFD) simulations, along with a lumped-mass mooring model and the actuator line model (ALM), are employed to capture the coupled fluid-structure interactions and mooring line dynamics. The results reveal significant differences in platform behavior, highlighting the impact of platform geometry on dynamic stability and mooring line response. The additional central column significantly improves pitch stability, reducing the maximum pitch angle by 38.7 % under combined wind and wave loading, indicating enhanced dynamic stability of the additional central column design. Additionally, an economic assessment is provided to evaluate the material costs, installation, and operational expenses for each platform type. The findings suggest that both configurations offer distinct advantages depending on operational and environmental conditions, contributing to the optimization of FOWT platform selection for future offshore wind farms.

1. Introduction

Floating wind turbines are increasingly recognized as a key solution for harnessing offshore wind energy, particularly in deep-water regions where traditional bottom-fixed turbines are impractical (Zou et al., 2024). Different floating platform configurations exhibit significant differences in structural stability, construction costs, transportation and installation complexity, mooring system investment, and operation and maintenance requirements. A comparative evaluation of these platforms is essential for informed decision-making, ensuring an optimal balance between technical performance and economic feasibility for the successful deployment of floating wind turbines.

Previous research has made significant progress in comparing various configurations of floating offshore wind turbine (FOWT) platforms. Thiagarajan and Dagher (2014) provided an overview of various floating platform designs, including ballast-stabilized (e.g., spar), mooring-stabilized, and buoyancy-stabilized (e.g., semi-submersible) types, discussing their stability mechanisms and global performance across different offshore conditions. Goupee et al. (2014) conducted 1:50 scale model tests of FOWT platform concepts, including a tension leg platform (TLP), a spar-buoy, and a semi-submersible, comparing their global motions, flexible tower dynamics, and mooring system responses. Matha (2010)performed a quantitative comparison of the responses of TLP, barge, and spar-buoy floating platforms using the fully coupled time-domain aero-hydro-servo-elastic simulation tool FAST with AeroDyn and HydroDyn. The study found that the barge platform exhibited the highest turbine loads, while the spar-buoy showed greater pitch and roll motions than the TLP but provided better stability in yaw. Similarly, Jonkman and Matha (2011) analyzed the dynamic responses of three FOWT concepts (TLP, spar-buoy, and barge) using FAST, revealing that the barge-supported turbine exhibited the highest loads, while the differences between the TLP and spar-buoy were relatively

* Corresponding author.
E-mail addresses: pengxuzou@gmail.com (P. Zou), jeremydb@umich.edu (J.D. Bricker).

https://doi.org/10.1016/j.oceaneng.2025.121615
Received 19 February 2025; Received in revised form 6 May 2025; Accepted 18 May 2025
Available online 27 May 2025

minor. Ioannou et al. (2020) conducted a cost analysis of three floater concepts (spar, barge, and semi-submersible), performing a parametric study on material thickness and manufacturing complexity. Li et al. (2022) carried out 1:60 scale physical model tests and coupled multi-body simulations of concrete and steel Y-shaped semi-submersible platforms, analyzing tower base loads and nacelle acceleration differences between the two structures.

Among the various floating platform designs, semi-submersible platforms have garnered significant attention due to their balance of stability, adaptability, and cost-effectiveness. These platforms rely on multiple buoyant columns for stability and maintain a relatively shallow draft, making them suitable for deployment across a broad range of water depths. Various semi-submersible concepts have been developed, with wind turbines either mounted on a center column or positioned on one of the offset columns. These two common configurations, the three-column design and the three-column with central column design, have been widely adopted. Notable implementations include the Fukushima V-Shape (Japan, 2015) (Ohta et al., 2013), WindFloat Atlantic (Portugal, 2020) (Adnan Durakovic), and Haizhuang Fuyao (China, 2022) (CSSC), which utilize the three-column design, while OO-Star (2011) (olavolsen, 2011), Fukushima Mirai (Japan, 2013) (Saeki et al., 2014), VolturnUS (2013) (Young et al., 2014), and Haiyou Guanlan (China, 2023) (Yihe) employ the three-column with central column configuration.

Although extensive research has been conducted on different floating platform configurations, a direct comparison between the three-column and three-column with central column semi-submersible platforms remains limited. Such a comparison is crucial for understanding their hydrodynamic performance, stability, and structural efficiency in FOWT applications. Existing studies often rely on simplified models that may not fully capture complex aero-hydro-mooring interactions.

Most previous research employs time-domain aero-hydro-servo-elastic simulation tools such as FAST or OpenFAST. These tools rely on potential flow theory for hydrodynamic predictions and blade element momentum (BEM) theory for aerodynamic calculations. Potential flow theory assumes inviscid, irrotational, homogeneous, and incompressible fluid behavior, necessitating additional damping coefficients based on experimental data to account for turbulence and viscosity effects. Similarly, the BEM method is semi-empirical, highly dependent on laboratory-scale experimental data, and has been shown to have limitations in unsteady aerodynamic predictions (Sebastian and Lackner, 2013). Hydrodynamic solvers such as ANSYS AQWA, ADAMS, and WAMIT, along with aero-servo-hydro-elastic codes like HAWC2, Sesam, and 3DFloat (Clement et al., 2021; Ding et al., 2018; Karimirad and Moan, 2012; Nygaard et al., 2016; Zhao et al., 2019), share similar limitations. These methods rely heavily on empirical data, making them insufficient for accurately estimating aero- and hydrodynamic loads on floating wind turbines in highly dynamic marine environments (Dunbar et al., 2015).

Computational fluid dynamics (CFD) has emerged as a high-fidelity, quantitative analysis tool capable of resolving significant aerodynamic unsteadiness and complex multi-physics interactions. Unlike simplified models, CFD can directly incorporate all relevant physical effects, including the interaction between blade tip vortices, tower vortex shedding, flow viscosity, wave diffraction and radiation, and wave slamming, without relying on empirical assumptions (Franke et al., 2004), (Alkhabbaz et al., 2024). In recent years, fully coupled aero- and hydro-dynamic FOWT models based on CFD have been developed (Cheng et al., 2019; Haider et al., 2024; Leble and Barakos, 2016; Liu et al., 2017; Pericas, 2022; Tran and Kim, 2016a; Zhang and Kim, 2018). These high-fidelity simulations enable detailed analysis of coupled aerodynamic and hydrodynamic behaviors under realistic operating conditions, offering significant improvements in accuracy compared to potential-based approaches. Yang et al. (2023) compared CFD with potential-based tools to evaluate the dynamic responses of FOWTs under severe operating conditions. Their results revealed that potential-based methods exhibited significant errors, particularly in predicting surge and pitch load responses. Similarly, Yang et al. (2024) identified notable discrepancies in integrated load analysis between CFD and potential flow-based tools, even when hydrodynamic coefficients were calibrated using free-decay tests. These findings support the growing trend of incorporating CFD tools in the design and analysis of next-generation FOWTs.

This study applies a coupled aero-hydro-mooring integrated simulation system using OpenFOAM to compare three-column and three-column with central column semi-submersible platforms. The primary objectives are (1) to evaluate the hydrodynamic, aerodynamic, and mooring dynamics of both platform configurations; (2) to analyze the motion responses of each design under realistic offshore wind and wave conditions; (3) to conduct an economic assessment of the two platform types considering material costs. Despite the extensive research on traditional semi-submersible platforms, the comparison and influence of geometric modifications—such as the addition of a central column—on platform dynamics remains underexplored. This study addresses that gap by performing a high-fidelity comparative analysis between a conventional three-column design and three-column with a central column configuration. The innovation of this work lies in combining a fully coupled CFD-RANS model with actuator line modeling to capture complex aero-hydro-mooring interactions under combined wave and wind conditions. By quantifying improvements in pitch and heave stability, the study provides practical design insights that support the development of more stable and cost-effective floating wind turbine platforms. These results are particularly valuable as the industry moves toward larger turbines and deeper water deployments, where platform dynamics become increasingly critical.

The paper is structured as follows: Section 2 describes the numerical methods used for different dynamic solvers. Section 3 introduces the FOWT configurations and presents numerical validation of the model. Section 4 provides a comparative analysis of the two platform types in terms of hydrodynamic, aerodynamic, and mooring dynamics. Section 5 presents an economic analysis of the two designs. Finally, Section 6 discusses the benefits and limitations of each configuration, providing insights for future development and deployment of floating wind turbines.

2. Methodology

2.1. Aerodynamic modeling

The actuator line model (ALM), introduced by Sørensen and Shen (2002), represents the turbine blades as virtual lines and divides them into discrete actuator points, similar to the BEM approach. The sectional aerodynamic forces acting on the blades are iteratively evaluated in an uncoupled manner and then projected onto the background grid surrounding the blade elements. The ALM was selected due to its balance between computational efficiency and physical accuracy in simulating turbine-induced flow fields. While ALM does not resolve blade geometry, it effectively captures the turbine wake and aerodynamic loading, making it suitable for coupled aero-hydro simulations. ALM methods have been extensively used in previous studies to predict wake flow characteristics, including wake expansion and radial flow, demonstrating their accuracy in wake flow simulations (Lin et al., 2019; Onel and Tuncer, 2021; Rai et al., 2017; Rocchio et al., 2020; Stevens et al., 2018).

In this study, the ALM implementation in the turbinesFoam library, developed by P. Bachant (Bachant et al., 2025), is integrated with OpenFOAM to simulate aerodynamic behavior. This approach provides high-fidelity flow velocity fields and detailed wake development characteristics while reducing computational costs by replacing complex blade geometries with virtual actuator lines.

The motion of the floating platform influences the relative wind experienced by the turbine blades, which in turn affects the aerodynamic forces applied by the actuator lines, subsequently influencing

platform motion. The relative wind velocity at each point along the actuator line is updated based on platform motion, as described by Eq. (1) (Cai et al., 2025) (Pericas, 2022).

$$\mathbf{U}_{\mathrm{rel}} = \mathbf{U}_0 + \Omega \times \mathbf{r} + \mathbf{U}_{\mathrm{r}} - \mathbf{U}_{\mathrm{p}} \tag{1}$$

where U_{rel} is the total relative velocity; U_0 is the inflow velocity vector; U_r is the component of the inflow velocity in the rotor plane; U_p is the airfoil velocity term due to the motion of the platform; $\Omega \times \mathrm{r}$ is the speed of airfoil caused by the blade's rotation.

The aerodynamic forces acting on the actuator element can be calculated using Eqs. (2) and (3) (Bachant et al., 2025)

$$F_\theta = \frac{\rho c |U_{rel}|^2}{2rd\theta dz}(c_l \sin\varphi - c_d \cos\varphi) \tag{2}$$

$$F_z = \frac{\rho c |U_{rel}|^2}{2rd\theta dz}(c_l \sin\varphi + c_d \cos\varphi) \tag{3}$$

where F_θ and F_z represent forcing term projected in the normal z and azimuthal θ directions; c is the local chord; ϕ is the inflow angle; C_l and C_d are the lift and drag coefficient, respectively.

To avoid singular behaviors and numerical instabilities, the aerodynamic forces are smoothed using a smearing function η, expressed as Eqs. (4) and (5) (Bachant et al., 2025)

$$\mathbf{f}_\varepsilon = \mathbf{f} \otimes \eta = (F_\theta, F_z) \otimes \eta \tag{4}$$

$$\eta = \frac{1}{\varepsilon^3 \pi^{3/2}} e^{-\left(\frac{d}{\varepsilon}\right)^2} \tag{5}$$

where f_ε is the smoothed aerodynamic force; f is the body force generated by the actuator elements; d is the distance between the measured point in flow field and the projected force application point in the actuator line model; ε is a constant parameter specifying the smearing width.

2.2. Mooring dynamics

The lumped mass method is applied to model the dynamic behavior of mooring lines. It discretizes a mooring line into multiple segments, where each segment consists of a lumped mass node connected by spring-damper elements. These lumped mass nodes are linked by segments that represent the mooring line's stiffness and damping properties, allowing the calculation of mooring line dynamic responses to forces from waves and currents. Each segment has tension properties based on the material and structural characteristics of the mooring line. By discretizing the line into a finite number of mass nodes, the lumped mass method reduces computational complexity compared to a fully continuous model, making it feasible for real-time or large-scale simulations.

In this study, the lumped mass method implemented in the open-source MoorDyn V2 is integrated with OpenFOAM to calculate mooring forces and account for the interaction between the mooring system and the floating platform (Hall, 2020). Mooring line tension calculated at each segment is defined as Eq. (6).

$$(T + C)_{i+\frac{1}{2}} = E\frac{\pi}{4}d^2\left(E(\varepsilon)\varepsilon_i + \frac{1}{2} + B(\dot{\varepsilon})\dot{\varepsilon}_{i+\frac{1}{2}}\right) \tag{6}$$

where T is axial stiffness, C is axial structural damping; E is Young's elastic modulus, d is the cable nominal diameter, ε is the segment strain, B is structural damping coefficient; $\dot{\varepsilon}$ is segment strain rate.

The complete equation of motion for each node i is given by Eq. (7)

$$[\mathbf{m_i} + \mathbf{a_i}]\ddot{\mathbf{r}}_\mathbf{i} = \mathbf{T}_{\mathbf{i}+\frac{1}{2}} - \mathbf{T}_{\mathbf{i}-\frac{1}{2}} + \mathbf{C}_{\mathbf{i}+\frac{1}{2}} - \mathbf{C}_{\mathbf{i}-\frac{1}{2}} + \mathbf{W_i} + \mathbf{B_i} + \mathbf{D_{pi}} + \mathbf{D_{qi}} \tag{7}$$

where m_i and a_i are node mass and hydrodynamic added mass, respectively; B_i is seabed contact force; r_i is node acceleration; D_{pi} and D_{qi} represent the transverse and tangential drag force, respectively.

Therefore, axial stiffness, internal damping forces, bending stiffness, line weight, buoyancy, seabed contact, and drag and inertia forces from Morrison's equation are considered.

2.3. Rigid body dynamics

In OpenFOAM, the "sixDoFRigidBodyMotion" solver is applied for rigid body motion simulations. This solver couples fluid dynamics with rigid body motion, allowing the simulation of structures subjected to external forces in the context of fluid-structure interaction (FSI). Its parameters are defined within the "dynamicMeshDict" dictionary. The "sixDoFRigidBodyMotion" solver solves the fully coupled translational and rotational motion equations for a rigid body in six degrees of freedom and accounts for hydrodynamic forces from the surrounding fluid, aerodynamic loads from the actuator line turbine model, gravity, buoyancy, and mooring system forces. The equations of motion are solved using a Newmark time integration scheme with added options for mass, damping, and restoring stiffness matrices. The solver allows dynamic mesh motion and is particularly suitable for simulating FOWTs subjected to complex environmental loading.

The external forces and moments are evaluated and defined with fluid loads, gravity and mooring forces. The fluid loads, including hydrodynamic and aerodynamic forces, are separated into viscous and pressure components and calculated at the body surface at every time step, as shown in Eqs. (8) and (9).

$$\mathbf{F} = \iint_s (p\hat{\mathbf{n}} + \underline{\tau})dS + \sum \mathbf{F_i} = \mathbf{F_p} + \mathbf{F_v} + \sum \mathbf{F_i} \tag{8}$$

$$\mathbf{M} = \iint_s \mathbf{r_{PR}} \times (p\hat{\mathbf{n}} + \underline{\tau})dS + \sum \mathbf{r_{iR}} \times \mathbf{F_i} + \sum \mathbf{M_i} = \mathbf{M_p} + \mathbf{M_v} + \sum \mathbf{r_{iR}} \times \mathbf{F_i} \tag{9}$$

where n is the identity matrix (normal vector), τ is the viscous stress tensor, $\mathbf{S}$ denotes the surface of the boundary patch for the rigid floating body. $\mathbf{F_i}$ is the tensor for the point forces, such as mooring force and gravity, and $\mathbf{r}_{PR}$ and $\mathbf{r}_{iR}$ represent the arms of hydrodynamic force and point force, respectively.

The relationship between motion and loads is governed by the rigid body equations. The motion is described in terms of the displacements and rotations of the center of mass as defined by the Newton-Euler equations. This can be expressed as a system of second-order differential equations, given by Eqs.10 and 11

$$m\ddot{\mathbf{d}} = \mathbf{F} \tag{10}$$

$$\underline{\mathbf{J}}\ddot{\phi} + \dot{\phi} \times (\underline{\mathbf{J}}\dot{\phi}) = \mathbf{M} \tag{11}$$

where m represents the total mass, $\mathbf{J}$ is the time-invariant inertia matrix relative to the center of mass, and d and ϕ denote the displacements and rotations of the rigid across all six degrees of freedom (DoFs).

By substituting the expressions for $\mathbf{F}$ and $\mathbf{M}$ into the Newton-Euler rigid body equations (Eqs. (8) and (9)), a system of ordinary differential equations (ODEs) is derived, where the motion state becomes the only remaining unknown.

2.4. Fluid flow governing equations

The dynamics of the fluid flow are governed by the incompressible Newtonian Navier-Stokes equations, which enforce the conservation of mass (continuity) and momentum. These equations describe the motion of the fluid within a control volume and are expressed as Eqs.12 and 13

$$\nabla \cdot \mathbf{u} = 0 \tag{12}$$

$$\frac{\partial \rho \mathbf{u}}{\partial t} + \mathbf{u} \cdot \nabla \rho \mathbf{u} = -\nabla p + \mu \nabla^2 \mathbf{u} + \mathbf{f} \tag{13}$$

where u is the velocity vector, t is time, p is the pressure, ρ is the density of the fluid, μ is the dynamic viscosity, f represents external forces.

In this study, the k-ω SST (Shear Stress Transport) turbulence model is applied to capture the turbulent characteristics of the flow. This model is a two-equation turbulence closure method based on the Reynolds-Averaged Navier-Stokes (RANS) equations. It combines the strengths of the k-ω model in the near-wall region and the k-ε model in the far-field flow, offering superior accuracy and robustness for a broad range of flows (Zou et al., 2023a), (Zou et al., 2023b). The equations can be expressed as Eqs. 14 and 15.

$$\frac{D}{Dt}(\rho k) = \nabla \cdot (\rho D_k \nabla k) + \rho G - \frac{2}{3}\rho k(\nabla \cdot u) - \rho \beta^* \omega k + S_k \tag{14}$$

$$\frac{D}{Dt}(\rho \omega) = \nabla \cdot (\rho D_\omega \nabla \omega) + \frac{\rho \gamma G}{\nu} - \frac{2}{3}\rho \gamma \omega(\nabla \cdot u) - \rho \beta \omega^2 - \rho(F_1 - 1)CD_{k\omega} + S_\omega \tag{15}$$

The turbulence viscosity is obtained using Eq. (16)

$$\nu_t = a_1 \frac{k}{\max(a_1 \omega, b_1 F_{23} S)} \tag{16}$$

where k is turbulence kinetic energy; ω is turbulence specific dissipation rate; S_k, S_ω are the source terms for k and ω, respectively; ν_t is turbulent eddy viscosity; F_1 and F_{23} are blending functions; S is the invariant measure of the strain rate; $\beta_1 = 0.075$; $\beta_2 = 0.0828$; $\gamma_1 = 5/9$; $\gamma_2 = 0.44$; $\beta^* = 0.09$, $a_1 = 0.31$, $b_1 = 1.0$.

The volume-of-fluid (VOF) method (Hirt and Nichols, 1981) is employed to accurately track the evolution of the air-water interface. This method is based on solving a continuity equation for the volume fraction σ of the i-th phase, which determines the fraction of the control volume occupied by each phase. The governing equation for the volume fraction is expressed in Eq. (17). To account for the presence of multiple phases within a grid cell, the fluid properties, such as viscosity μ and density ρ, are reconstructed using a volume-weighted averaging approach. This reconstruction is carried out based on the phase volume fractions, as detailed in Eqs. 18 and 19.

$$\frac{\partial \sigma}{\partial t} + \mathbf{u} \cdot \nabla \sigma = 0 \tag{17}$$

$$\rho = \sum_{i=1}^{n} \sigma_i \rho_i \tag{18}$$

$$\mu = \sum_{i=1}^{n} \sigma_i \, \mu_i \tag{19}$$

where σ_i is the volume fraction of the ith phase, and v_i is the velocity of the ith phase.

By averaging the phase properties within each computational cell, the method ensures a smooth transition between phases and maintains numerical stability at the interface. In addition, waves2Foam library, developed by Jacobsen (Jacobsen et al., 2012) is applied for wave generation and absorption.

2.5. Model coupling

As introduced in Section 2.3, in a fluid-structure interaction simulation, OpenFOAM computes the body surface forces and moments at each time step and updates the rigid body motion via a PIMPLE outer-corrector loop. The resulting motion of the body is then updated, influencing the fluid flow in subsequent iterations. The coupling between the lumped-mass mooring model and OpenFOAM's dynamic mesh solver follows a loose-coupling strategy, effectively integrating mooring dynamics with fluid-structure interactions. At the start of each time step, the platform's position and velocity, determined from the dynamic mesh motion, are transmitted to the mooring model. The mooring model solves the mooring line dynamics over multiple sub-steps within the OpenFOAM time step, accurately capturing fairlead kinematics and line tensions. The calculated mooring forces are subsequently fed back into OpenFOAM as external forces applied to the platform, influencing its motion. This iterative exchange ensures consistency between platform dynamics and mooring responses while maintaining computational efficiency and modularity. The approach captures the rapid dynamics of mooring lines without requiring tight coupling, making it well-suited for complex fluid-structure interaction simulations.

In the ALM calculation step, the turbine's position and velocity are updated based on the rigid body's motion state in the current iteration. The resulting aerodynamic loads are applied as external constraints on the rigid body during the next PIMPLE iteration. In this context, the PIMPLE scheme not only couples the rigid-body and fluid equations but also incorporates the ALM rotor dynamics. To achieve adequate rotor-platform coupling, the number of outer correctors was set to nOuterCorrectors = 3.

3. Numerical model set-up

3.1. Model description

The FOWT system comprises three primary components: the mooring system, the wind turbine system, and the floating platform. In this study, the NREL 5 MW horizontal-axis reference wind turbine (Jonkman et al., 2009) is employed, with a hub height of 87.6 m above the still water level (SWL). The key properties of the wind turbine are summarized in Table 1.

To ensure a direct comparison of the dynamic responses between the two platform configurations, the displacement volume is maintained constant, thereby preserving similar buoyancy and stability characteristics under identical loading conditions. Both platforms are constructed using concrete with a density of 2400 kg/m^3, with a uniform wall thickness of 300 mm. Additionally, the draft depth and freeboard length are identical for both configurations, ensuring comparable above-water and submerged loading conditions.

For the three-column configuration, the wind turbine tower is cantilevered atop one of the offset columns. In contrast, in the three-column platform with a central column, the turbine tower is positioned on the central column. The offset columns in both configurations are interconnected by three pontoons at the base, without additional braces. To achieve the prescribed draft and displacement volume, the pontoons and offset columns are filled with ballast water. For clarity, the three-column platform with a central column is designated as **Platform 1**, while the conventional three-column configuration is labeled **Platform 2**. The design process for a floating wind turbine platform begins by defining initial inputs such as the turbine capacity and platform self-weight. Based on these, the required buoyancy is determined to ensure the platform can support the combined weight of the turbine, platform, and

Table 1
Wind turbine parameters (Jonkman et al., 2009).

Rated power (MW)	5
Rotor Orientation, Configuration	Upwind, 3 Blades
Hub height (m)	87.6
Integrated Tower Mass	249,718 kg
Rotor diameter (m)	126
Rotor Mass	110,000 kg
Nacelle Mass	240,000 kg
Cut-In, Rated, Cut-Out Wind Speed	3 m/s, 11.4 m/s, 25 m/s

auxiliary systems. Preliminary structural dimensions—including column diameter, draft, and spacing—are then estimated. A hydrostatic stability check follows, calculating parameters such as the metacentric height (GM) and restoring moment to ensure sufficient initial stability. This process is iterated by adjusting the platform geometry and spacing. Detailed specifications of both floating platforms are provided in Table 2 and illustrated in Fig. 1.

To ensure a fair performance comparison between the three-column and three-column with central column semi-submersible FOWT platforms, the mooring system type and configuration are kept identical. In this study, a three-line catenary mooring system is employed, with each line connected to an offset column at a uniform horizontal angle of 120° between adjacent lines. The mooring line length is determined based on maintaining consistent pretension levels. The fairleads are positioned at the outer edges of the three offset columns, 13.5 m below the still water level (SWL), for both platforms, while the anchors are placed at a depth of 200 m below the SWL. The detailed mooring parameters for both configurations are provided in Table 3.

3.2. Model set-up

To simplify the model, the detailed components of the hub, nacelle, and tower are omitted in the actuator line model. The computational domain measures 915 m in length, 686 m in height, and 378m in width, with the FOWT center positioned 343 m from the inlet and 572 m from the outlet boundaries. A logarithmic wind profile (Fig. 2) is prescribed at the inlet to define the velocity boundary of the airflow with a turbulence intensity of 2 %, following Eq. (20) (Cai et al., 2025) (Pericas, 2022).

$$\frac{v_2}{v_1}=\frac{\ln(h_2-d)-\ln z_0}{\ln(h_1-d)-\ln z_0} \tag{20}$$

where h_1 is height, h_2 is hub height (i.e., 90 m), v_1 is the wind speed at height h_1, v_2 is the wind speed at height h_2 (11.4 m/s), d is the terrain displacement height factor, and z_0 is the surface roughness length, which is set to 0.5m (Cai et al., 2025) (Pericas, 2022).

Additionally, a second-order Stokes wave is imposed at the inlet boundary to represent the water phase. At the outlet, a zero-gradient velocity condition is applied, while the platform surface follows a no-slip, hydraulically smooth wall condition. Symmetry (free-slip) boundary conditions are enforced at the top and bottom to mitigate wall effects. To allow platform motion, a "movingWallVelocity" boundary condition is applied within a localized mesh region of 120 m × 120 m × 60 m. To minimize wave reflection at the computational domain boundaries, relaxation zones were implemented at both the inlet and outlet regions. These zones gradually blend the numerical solution with a prescribed target solution over a specified distance, effectively damping incoming wave energy. In this study, the relaxation zones were set to a length of 1 time and 2 times the incident wavelength were implemented at inlet and outlet, respectively, which is sufficient to absorb reflected waves without significant re-reflection into the computational domain (Cai et al., 2025) (Cheng et al., 2019). The computational domain is shown in Fig. 3.

The computational domain is subdivided into three regions (Fig. 4). The background mesh resolution is 6.4 m in the x- and y-directions and 3.7 m in the z-direction. A refined mesh near the water surface, with a resolution of 0.4 m × 0.4 m × 0.23 m, ensures accurate wave propagation modeling. Additional mesh refinement with a resolution of 1.6m is applied around the platform and turbine wake to capture key flow features. The total computational domain comprises 6.45 million grid cells. The simulation employs an initial time step of 0.001 s with adaptive time stepping and is run for 300 s. All computations were performed on a server equipped with an AMD EPYC 9684X processor (96 cores, 768 GB RAM). The total simulation time required to generate the results was approximately 15 days using 64 CPUs.

To ensure the accuracy and reliability of the CFD simulation results, a mesh independence study was conducted. Three different mesh densities were evaluated, with total cell counts of approximately 4.2 million (Coarse mesh), 6.45 million (Medium mesh), and 8.1 million (Fine mesh). Key response parameters including platform surge motion and thrust coefficient at 50~100s were monitored and compared across these mesh configurations (see Fig. 5). The results showed that increasing the mesh density beyond 6.45 million cells led to less than 2 % variation in these key quantities, indicating that the solution had converged with respect to mesh size. Based on this analysis, the mesh with 6.45 million cells was selected for all subsequent simulations, as it offered a good balance between numerical accuracy and computational efficiency.

3.3. Numerical validation

The accuracy of the numerical model was validated through simulations of the benchmark 5 MW OC4-DeepCwind FOWT (Robertson et al., 2014). The semi-submersible platform comprises a central main column supporting the turbine tower, connected to three offset columns via cross members. Uzunoglu and C. Guedes Soares (Uzunoglu and Guedes Soares, 2015) compared the dynamic response between a full 3D geometric model of FOWT platform and a model omitting the connecting bracing, and it shows similar results under combined waves and winds. Therefore, to simplify the model, the connecting braces are omitted. The platform extends 10 m above and 20 m below the still water level, with a total mass of 1.3473×10^7 kg. The offset columns are spaced 50 m apart. The mooring system consists of three catenary mooring lines arranged at 120° intervals. Fairleads are positioned at the tops of the base columns, 14 m below the SWL, while anchors are placed at a depth of 200 m. Detailed platform and mooring line properties are shown in Table 4 (Robertson et al., 2014).

The coupled aero-hydro-mooring system for the OC4 platform is simulated under combined wave and wind conditions. The environmental conditions include: a wind speed of 11.4 m/s, and a regular wave characterized by a wave height of 7.58m and wave period of 12.1s. The turbine is operating with a 12.1 rpm rotational speed. The simulated surge, heave, and pitch responses of the OC4 platform are compared with results from previous studies, as shown in Fig. 6. The present surge motion amplitudes align closely with the findings of Cai et al. (2025), whereas Haider (Haider et al., 2024) reports smaller surge motions. In terms of mean motion values, the present pitch results fall between those of previous studies. The present pitch and heave motions show generally good agreement with Haider et al. (2024). However, a significant discrepancy is observed when compared to the results reported by Cai et al. (2025). This difference is likely attributed to variations in model properties and mooring line parameters. Specifically, the mass density of the mooring lines in Cai et al.'s study is 108.63 kg/m, whereas both Haider et al. and the present study use a value of 113.35 kg/m. Additionally, in this study, we adopted a transverse drag coefficient of 1.1 and a transverse added mass coefficient of 1.0 for the mooring lines, following the recommendations of Robertson et al. (2014). In contrast,

Table 2
Platform properties.

	Platform1	Platform 2
Depth of platform base below SWL (total draft) (m)	20	20
Elevation of central column (tower base) above SWL (m)	8	/
Elevation of offset columns above SWL (m)	10	10
Spacing between offset columns (m)	55	68
Diameter of central column (m)	6.5	/
Diameter of offset columns (−)	5.5	4.5
Height of pontoons(m)	6	5
Platform mass, including ballast (kg)	1.1E+7	1.1E+7
CM location below SWL (m)	14.24	15.56
Cut Water Plane Area (m^2)	315.42	188.32
Platform pitch/roll inertia about CM ($kg{\cdot}m^2$)	4.14E+9	5.61E+9
Platform yaw inertia about CM ($kg{\cdot}m^2$)	6.93E+9	1.02E+10

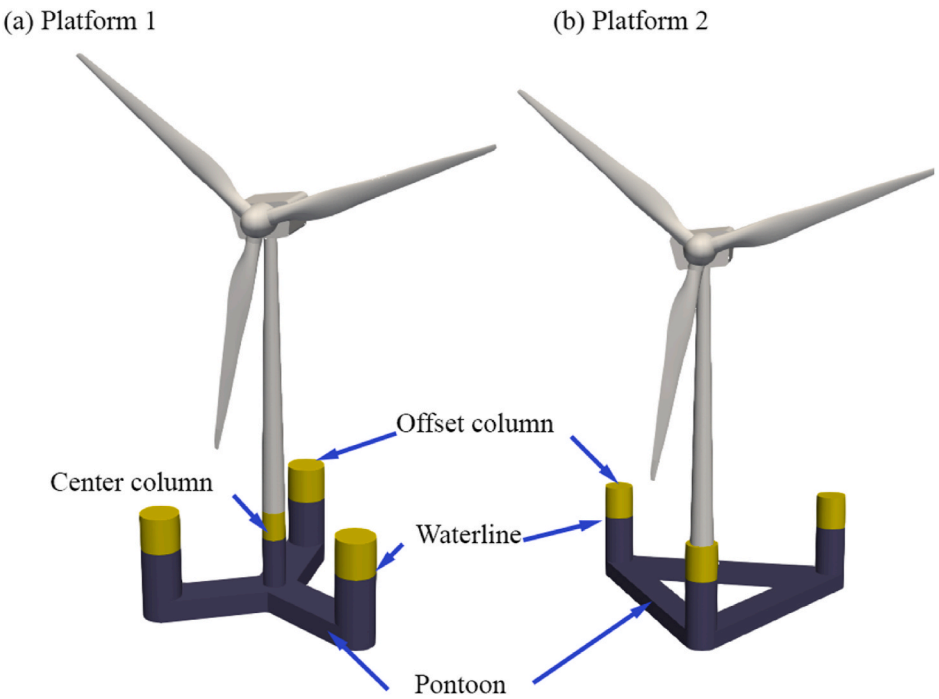

Fig. 1. Schematic diagram of the FOWTs. (a) Platform 1; (b) platform 2.

Table 3
Mooring line properties.

Diameter (m)	0.0766
Mass in length (kg/m)	108.63
Axial stiffness EA(N)	753.6E+6
Breaking strength (N)	3044.36E+3
Pre-tension (kN)	880
Line length – platform 1 (m)	843.5
Line length – platform 2 (m)	837

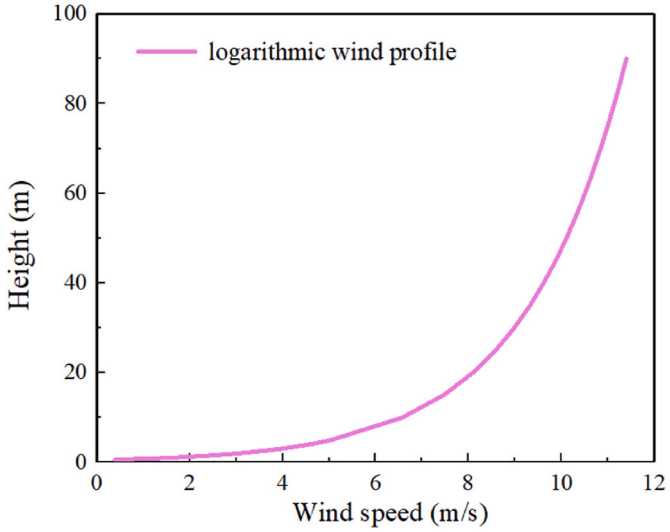

Fig. 2. Logarithmic wind profile at the inlet with height.

Haider et al. applied a transverse drag coefficient of 2.0 and an added mass coefficient of 0.8. These hydrodynamic coefficients can affect the damping characteristics and dynamic response of the platform. Overall, the comparison demonstrates good agreement, validating the reliability of the numerical model.

The comparison of mooring line tensions is presented in Fig. 7. Mooring line 1 is aligned with the incident wave direction at the upstream side, while mooring lines 2 and 3 are symmetrically positioned on the downstream side (Fig. 3). Due to their symmetrical distribution along the x-axis, mooring lines 2 and 3 exhibit nearly identical tension responses; therefore, only the tensions of mooring lines 1 and 2 are analyzed. Given its alignment with the wave direction, mooring line 1 experiences the highest tension forces among all lines. The mean mooring tensions obtained from the present simulations are 1738.24 kN for line 1 and 726.57 kN for line 2, indicating that the mean tension in line 1 is approximately 2.4 times that of line 2. A comparison with previous studies reveals that the simulated mooring tension for line 1 deviates by 3.51 % from the results reported by Haider et al. (2024) and by 12.71 % from those of Cai et al. (2025). For mooring line 2, the present results show a difference of 19.69 % compared to Haider et al. (2024) and 5.47 % compared to Cai et al. (2025). These variations may be attributed to differences in mooring system implementations.

The aerodynamic performance predictions, including aerodynamic thrust and rotor aerodynamic power responses of the FOWT, are presented in Fig. 8. The aerodynamic response exhibits a predominantly sinusoidal pattern, with a fluctuation period matching the wave period. For rotor aerodynamic power, the deviations are 8.34 % and 5.31 % compared to Haider et al. (2024) and Tran and Kim (2016b), respectively. The average thrust force obtained from the present simulations deviates by 1.91 % compared to Haider et al. (2024) and by 2.93 % compared to Tran and Kim (2016b). The phase shift observed in both the power and thrust curves compared to previously published studies is primarily attributed to differences in the computational domain length. This discrepancy in wave travel time introduces a temporal offset in the onset of wave-structure interactions, resulting in a consistent phase difference relative to studies with different wave arrival times. In addition, the wind inflow properties including turbulence, shear and veer, and wave-induced wind fluctuations can cause the differences of power and thrust phase.

Overall, the numerical results from the present model demonstrate good agreement with previous studies, including platform motion responses, mooring forces, and aerodynamic characteristics. This consistency validates the reliability of the model for further analysis.

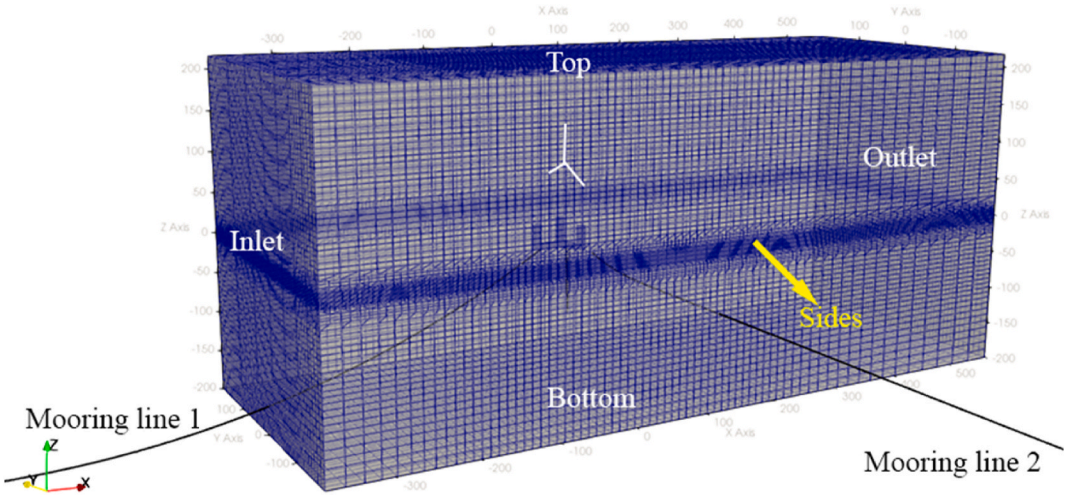

Fig. 3. Mesh configuration in full domain.

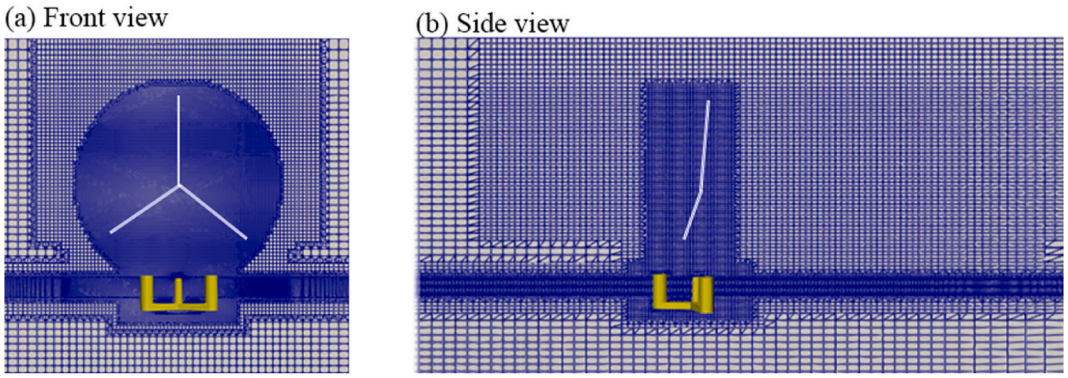

Fig. 4. Mesh configuration. (a) Front view; (b) side view.

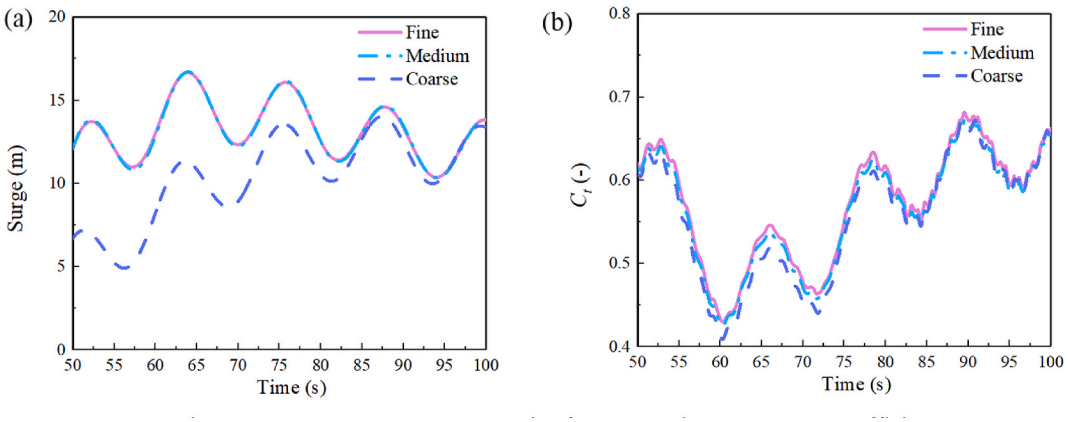

Fig. 5. Mesh convergence analysis of surge motion and thrust coefficient.

4. Results analysis

4.1. Free decay test

To investigate the natural frequencies in different motion directions, moored free-decay simulations were conducted for the two semi-submersible foundations under quiescent conditions, with no wind, wave, or current loads. The fluid was initialized in a fully static state before the platforms were released. Initial displacements or rotation angles were applied to the platforms, and the resulting motion amplitudes were normalized by their respective initial displacements.

Fig. 9(a) and 10(a) present the free-decay response time histories for the heave and pitch degrees of freedom. The damping ratio ζ of the FOWT system is determined using Eq. (21).

$$\zeta = \frac{1}{2\pi} \ln \frac{A_i}{A_{i+1}} \tag{21}$$

where A_i and A_{i+1} are the oscillation amplitude at the ith and $(i+1)^{th}$

Table 4
OC4-DeepCwind platform properties (Robertson et al., 2014).

Platform mass (kg)	1.3473 E+7
Center of mass below waterline (m)	10.20754
Total roll inertia (kg m^2)	1.31657E+10
Total pitch inertia (kg m^2)	1.31657E+10
Total yaw inertia (kg m^2)	1.90647E+10
Draft (m)	20
Unstretched line length (m)	835.35
Mooring line diameter (m)	0.0766
Mass in length for mooring line (kg/m)	113.35
Axial stiffness for mooring line (N)	753.6E+6
Transverse drag coefficient (−)	1.1
Transverse added mass coefficient (−)	1.0
Tangential drag coefficient (−)	0.05
Tangential added mass coefficient (−)	0

period, respectively.

The damping ratios for Platforms 1 and 2 in heave motion are 0.036 and 0.097, respectively, while in pitch motion, they are 0.016 and 0.082, respectively. The significantly higher damping ratio of Platform 2 in both heave and pitch degrees of freedom suggests that the additional central column enhances the overall stiffness of the FOWT system. This increased stiffness reduces the platform's flexible vibration amplitude in the fluid flow, thereby diminishing the damping effect.

The time-history curves of the free-decay motions were transformed into frequency domain through Fast Fourier Transform (FFT) transformation (see Fig. 9(b) and 10(b)), to reveal how energy distributed across different frequencies. The peak frequencies of the response spectrum correspond to the natural frequencies of the floating platforms in the respective degrees of freedom.

The natural frequencies of Platform 1 in heave and pitch motions are

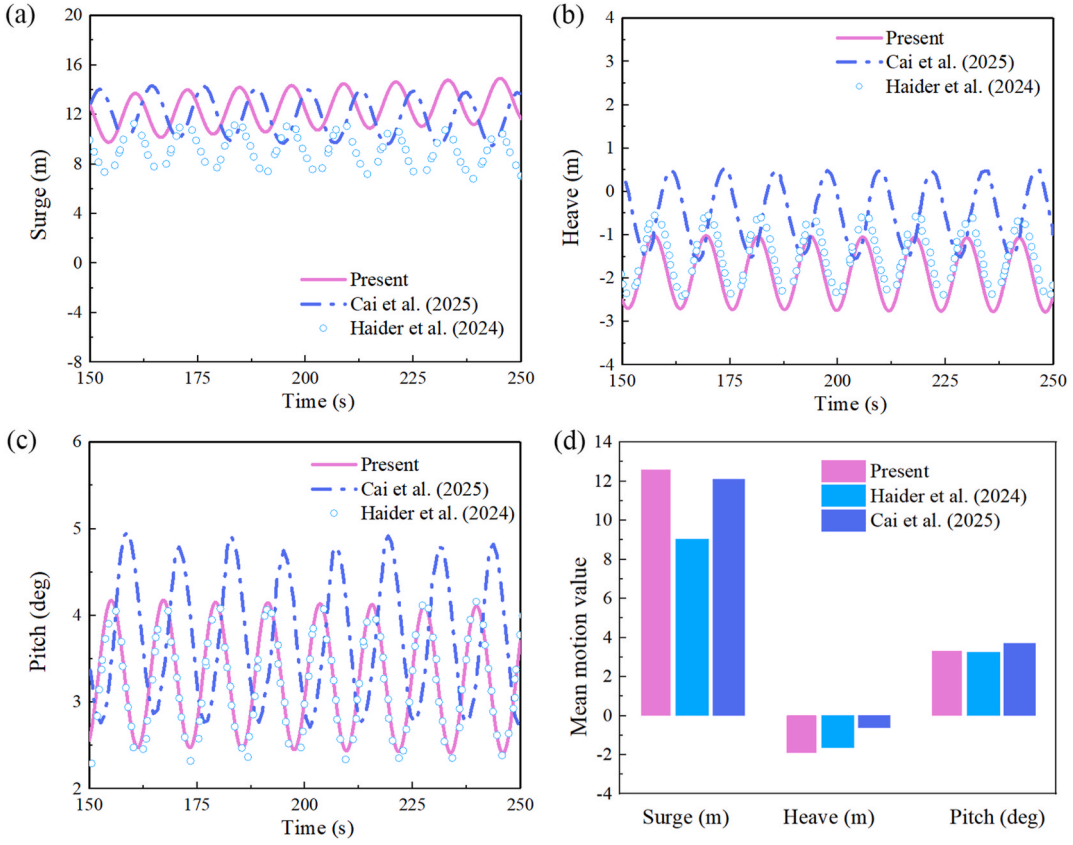

Fig. 6. Comparisons of the motion response of the FOWT.

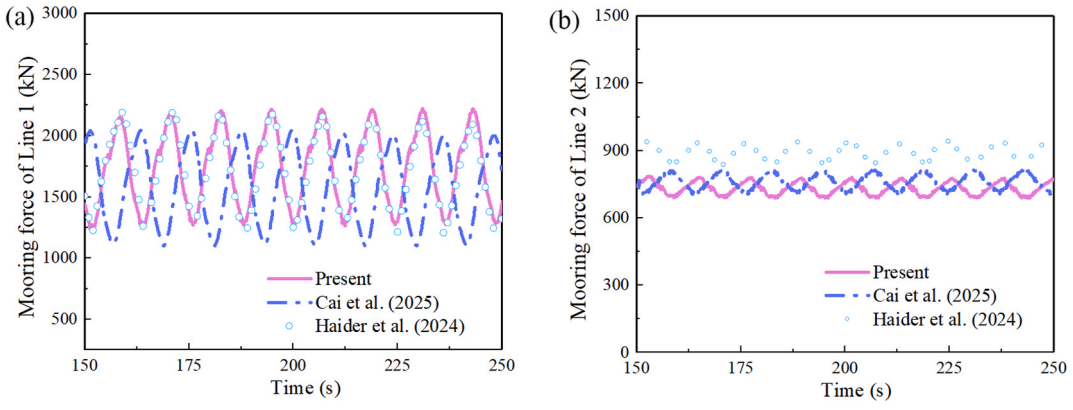

Fig. 7. Comparisons of the mooring dynamics of the FOWT.

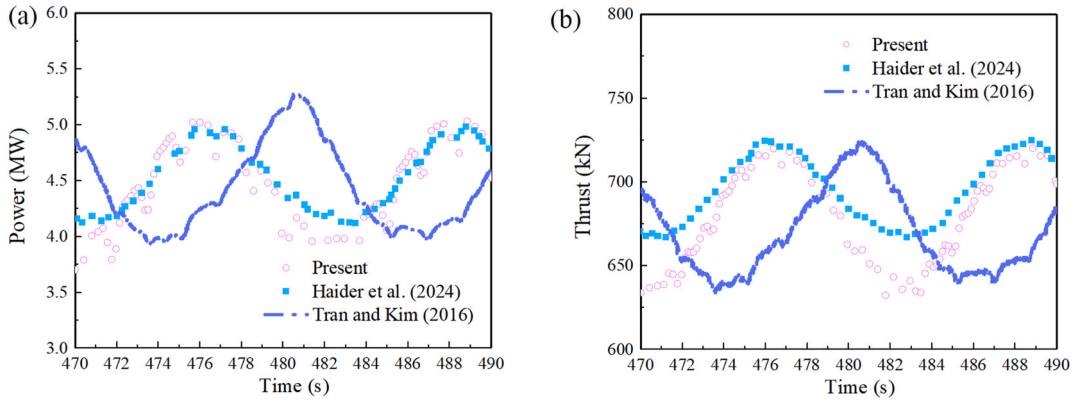

Fig. 8. Comparisons of the aerodynamics of the FOWT.

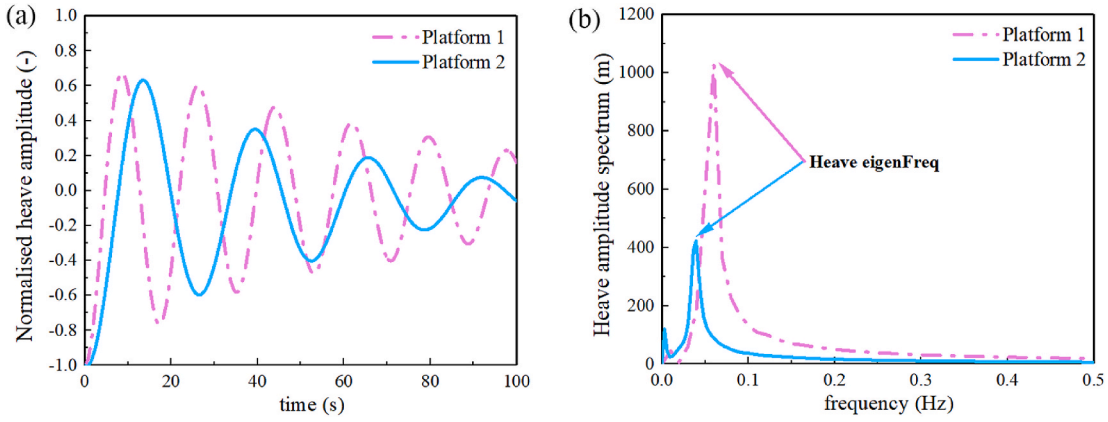

Fig. 9. Free decay of heave motion. (a) time-domain; (b) frequency-domain.

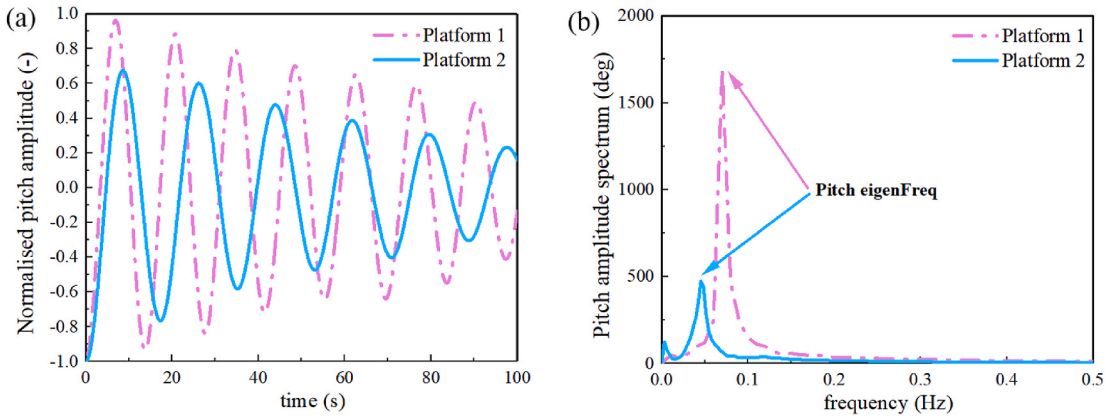

Fig. 10. Free decay of pitch motion. (a) time-domain; (b) frequency-domain.

0.055 Hz and 0.070 Hz, respectively, while for Platform 2, they are 0.039 Hz and 0.045 Hz, respectively. These results indicate that Platform 2 exhibits lower natural frequencies in both heave and pitch, effectively reducing the risk of resonance with low-frequency waves. Additionally, the peak values of the heave and pitch amplitude spectra for Platform 1 are significantly larger than those for Platform 2. A larger peak value indicates a more pronounced vibration response for Platform 1 in these frequency ranges.

A low-frequency peak is also observed in the heave and pitch amplitude spectra for both platforms, corresponding to the surge natural frequencies. This can be attributed to the stiffness provided by the mooring system. The two distinct spectral peaks suggest dynamic coupling effects between surge and pitch motions.

4.2. *Hydrodynamic performance*

In this study, a thorough examination on how different platform configuration affects the dynamic performance of the FOWT is investigated. The coupled aero-hydro-mooring system for both types of FOWTs was simulated under combined wave and wind conditions. To evaluate the performance of both proposed platforms under realistic operating scenarios, we conducted simulations for two representative wave-wind

cases under operational conditions. In both cases, the wind speed was set to 11.4 m/s, which corresponds to the rated wind speed of the reference wind turbine. The wind inflow is assumed to be uniform with a turbulence intensity of 2 %. This choice ensures that the turbine operates at its maximum aerodynamic efficiency, providing a meaningful assessment of platform performance under typical energy production conditions. The turbine operates at fixed tip-speed ratio (TSR) of 7.0. The associated wave conditions were selected based on commonly encountered sea states for moderate operational environments. A second-order Stokes wave is chosen in this study to systematically evaluate and compare the hydrodynamic performance of the two semi-submersible platform configurations under combined wind and wave conditions. Regular waves provide a simplified and consistent loading environment that allows for clearer interpretation of platform responses—such as pitch motion, mooring tension variation, and wake development—without the added complexity of random wave components. The load cases are outlined in Table 5.

The wave simulation duration is set to 300 s. Time histories of the hydrodynamic responses (surge, pitch, and heave) for both platforms under these conditions are presented. To eliminate transient effects, the analysis focuses on the zoomed-in data from the 200–300s interval, as shown in the subfigures. Additionally, the time-domain signals for surge, heave, and pitch motions of the two platforms are transformed into frequency-domain signals using FFT for further analysis, as shown in Figs. 11–13.

Fig. 11(a) displays the surge motion responses for both platform types in the time domain. Between 200 and 300 s in Case 1, the surge motion amplitudes for Platform 1 and Platform 2 are 3.30 m and 2.87 m, respectively, with maximum surge motions of 17.65 m and 16.87 m. In Case 2, the surge motion amplitudes for Platform 1 and Platform 2 are 1.64 m and 1.36 m, respectively, with corresponding maximum surge motions of 15.87 m and 15.30 m. Overall, the motion amplitudes of Platform 1 in both load cases are larger than that of Platform 2. This can be attributed to Platform 1's greater number of columns and smaller spacing, which results in a larger wave action area and increases the horizontal wave forces acting on the structure. Consequently, Platform 1 is more sensitive to horizontal loads induced by the waves, leading to larger horizontal motion responses.

In the frequency domain analysis (Fig. 11(b)), two distinct peaks are observed for both load cases. The first peak corresponds to the natural frequency in surge, while the second peak represents the wave frequency. For Platform 1, the first peaks are located at 0.009 Hz and 0.003 Hz for Platforms 1 and 2, respectively, while the second peaks occur at 0.083 Hz and 0.1 Hz for the two load cases, corresponding to wave periods of 12.1s and 10s, respectively. Notably, in Case 2, the first peaks of both platforms become broader and flatter, rather than being sharply concentrated at a single frequency. This phenomenon arises from the limited frequency resolution of the FFT due to the relatively short signal duration, which prevents the separation of closely spaced frequency components. Additionally, possible frequency drift, amplitude modulation, or unstable periodicity in the time-domain signals can cause the dominant frequency energy to spread over a broader frequency band.

Fig. 12(a) illustrates the heave motion responses of the platforms in the time domain. The heave response of Platform 2 is higher than that of Platform 1 in both load cases. In Case 1, the heave motion amplitudes for Platform 1 and Platform 2 are 2.44 m and 2.89 m, respectively, with Platform 1 exhibiting a 16 % smaller heave amplitude. This can be attributed to Platform 1's larger waterplane area (due to the larger offset column diameter and the additional central column), which provides higher heave stiffness and greater restoring force in heave motion. As a result, the heave response of Platform 1 is reduced. Similarly, in Case 2, the heave motion amplitudes for Platform 1 and Platform 2 are 1.31 m and 1.48 m, respectively, with Platform 1 exhibiting a 11 % smaller heave amplitude. With increasing wave height and period, the difference in heave motion amplitude between the two platforms becomes more pronounced. In the frequency domain analysis (Fig. 12(b)), the peak values for Platform 1 are 0.055 Hz (corresponding to the natural frequency in heave motion) and 0.083 Hz for Case 1 and 0.1 Hz for Case 2 (corresponding to the wave frequencies). For Platform 2, the peak frequency represents heave natural frequency is located at 0.039 Hz.

Fig. 13(a) presents the pitch motion responses of the two platform types for both load cases in the time domain. In Case 1, the pitch motion amplitudes for Platform 1 and Platform 2 are 3.72° and 3.84°, respectively, with maximum pitch angles of 4.52° and 7.40°, respectively. In Case 2, the pitch motion amplitudes for Platform 1 and Platform 2 are 1.80° and 2.81°, respectively, with maximum pitch angles of 4.20° and 7.04°, respectively. The pitch motion amplitude of Platform 1 is smaller than that of Platform 2 for both load cases. The maximum pitch angle of Platform 2 being approximately 1.64 times greater than that of Platform 1 for both load cases. The additional central column significantly improves pitch stability, reducing the maximum pitch angle by 38.7 % under combined wind and wave loading. This difference can be attributed to Platform 1's more uniform buoyancy and center of gravity distribution, despite having the same displacement volume. Additionally, Platform 1's larger waterplane area and stronger hydrostatic pitch restoring moment effectively suppress pitch motion.

In the frequency domain analysis (Fig. 13(b)), multiple distinct peaks can be observed for Platform 1. The peak values correspond to 0.009 Hz (natural frequency in surge motion), 0.07 Hz (natural frequency in pitch motion), and 0.083 Hz for Case 1 and 0.1 Hz for Case 2 (wave frequencies), indicating coupled dynamics between pitch and surge motions. The low-frequency peak corresponds to surge resonance, influenced by the floating structure's low natural frequency in the surge mode. Surge motion indirectly excites pitch due to coupling effects, which results in the first peak in the pitch response. The middle frequency peak represents the natural frequency of pitch motion, primarily determined by the platform's hydrostatic restoring moment, added mass, and inertia. At this frequency, the pitch response is dominant, although surge motion may still contribute due to coupling effects. The high-frequency peak is related to wave-induced excitation, which occurs near or above the wave frequency. At these frequencies, the dynamic responses of the structure are driven by external wave forces, exciting both pitch and surge motions, although the system typically does not resonate.

The presence of three distinct peaks underscores the importance of coupled hydrodynamic analysis when designing floating structures, particularly highlighting the interaction between rotational and translational dynamics. For Platform 2, the natural frequency in pitch motion is 0.045 Hz. Additionally, from Fig. 13(b), it is evident that the amplitude of the spectrum at the platform's natural frequency is smaller than that at the wave frequency. Furthermore, the wave frequency response of Platform 1 is significantly lower than that of Platform 2.

Interestingly, it can be observed that for both load cases, surge and heave motions generally exhibit a consistent phase relationship (see Fig. 11(a) and 12(a)), while a phase deviation is evident in the pitch motion of the two platforms (Fig. 13(a)). This discrepancy arises primarily because surge and heave motions are predominantly influenced by wave forces, whereas pitch motion is significantly affected by moments of inertia, damping, flotation characteristics, and wave-induced moments. Variations in the center of gravity and buoyancy positions between the two platforms lead to differences in the pitch moment of inertia, resulting in a phase deviation in the pitch motion.

Table 5
Load case properties.

Load case	Case 1	Case 2
Inflow wind speed (m/s)	11.4	11.4
Rotor speed (rpm)	12.1	12.1
Wave height (m)	7.58	6
Wave period (s)	12.1	10

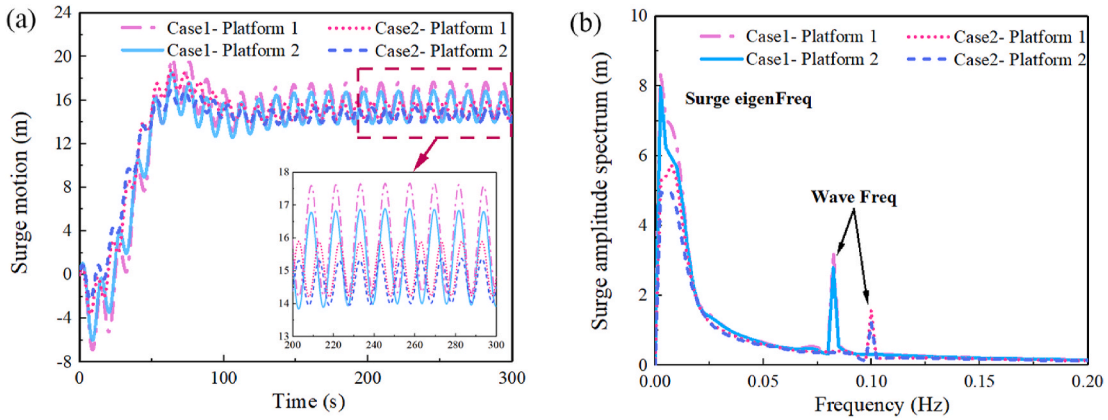

Fig. 11. Surge motion response of the two platforms. (a) Time-domain; (b) frequency-domain.

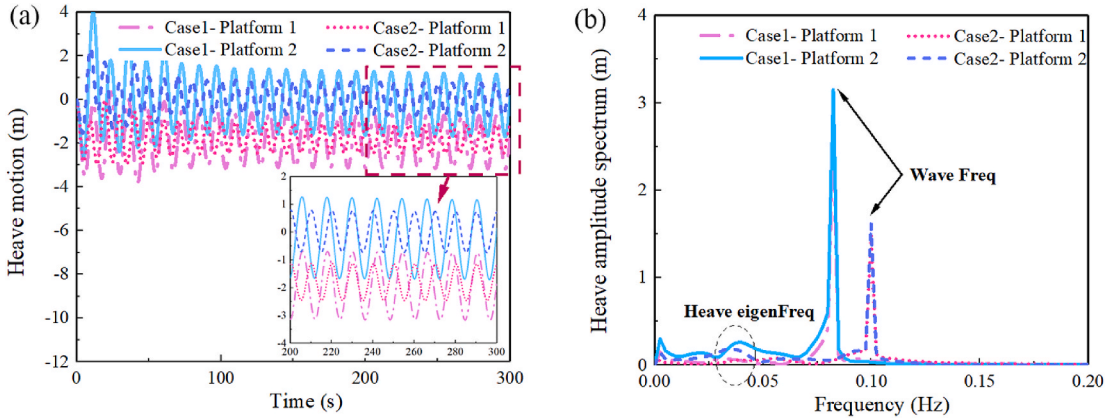

Fig. 12. Heave motion response of the two platforms. (a) time-domain; (b) frequency-domain.

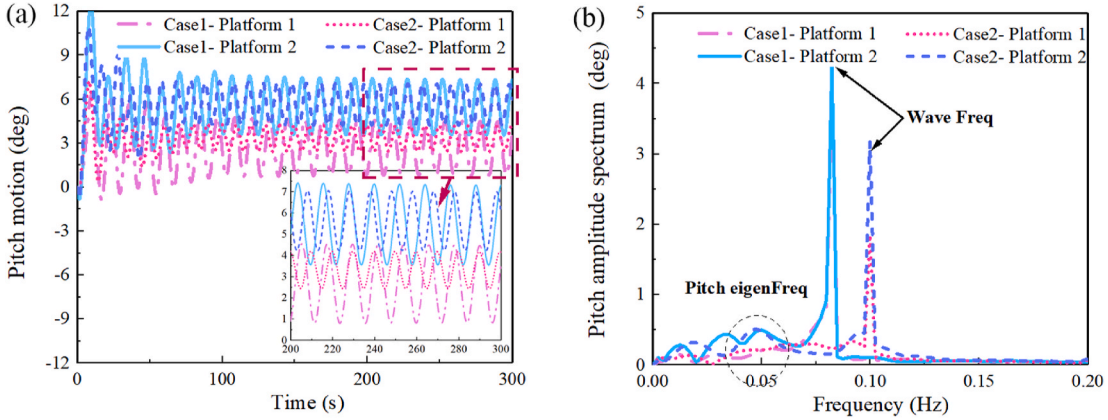

Fig. 13. Pitch motion response of the two platforms. (a) time-domain; (b) frequency-domain.

4.3. Aerodynamic performance

The variation in dynamic thrust force and rotor aerodynamic power for the two platforms in both load cases is shown in Fig. 14. The mean thrust force and power generation are generally similar for both platforms. However, Platform 2 exhibits larger fluctuations. For instance, in Case 2, the mean variation amplitude in rotor aerodynamic power for Platform 1 and Platform 2 are 2.26 MW and 2.80 MW, respectively. The mean variation amplitude in thrust force for Platform 1 and Platform 2 are 147.71 kN and 161.56 kN, respectively. This disparity is primarily due to the larger pitch motion of Platform 2, with greater pitch amplitude leading to more intense fluctuations in aerodynamic performance.

Comparing Case 1 and Case 2, it is evident that the amplitude of power fluctuations increases significantly with higher wave heights. This is because larger waves induce stronger platform pitch and heave motions, which in turn amplify variations in the relative wind speed experienced by the rotor plane. As a result, transient peaks in wind speed leads to greater instantaneous power output. However, the average power decreases due to excessive platform attitude disturbances that cause the rotor to deviate from the optimal inflow angle, reducing energy capture efficiency. Similarly, increased wave height intensifies

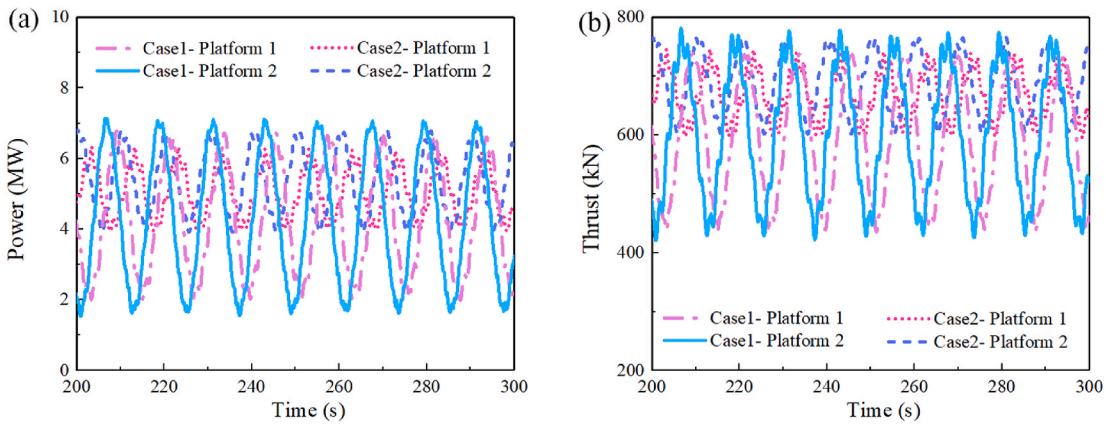

Fig. 14. Aerodynamic characteristics of the two platforms. (a) Rotor aerodynamic power; (b) thrust.

platform motion, altering the inflow angle and thereby enhancing thrust fluctuations. Nevertheless, the amplified motion also impairs inflow efficiency, leading to a reduction in average thrust. It can also be observed that phase deviations exist between the power and thrust curves for the two platforms. This phase difference is attributed to the phase shift in pitch motion and the differing positions of the wind turbines on the platforms.

Tip vortices are generated when high-pressure air from the bottom of the blade tip spills over into the low-pressure region above the blade, creating a rotational wake. Additionally, the turbine experiences motion induced by periodic wave forces, which alters the relative velocity and angle of attack on the blade, leading to periodic variations in blade aerodynamics and vortex shedding behavior. These motions can cause vortex tubes to either group together or spread apart, resulting in non-uniform vortex spacing. The wake vortex of the rotor is visualized using the iso-surface of the second-order invariant of the rate of strain tensor, Q = 0.01, and the velocity magnitude is shown at four representative time instants across one wave period (see Fig. 15) for both platforms. A distinct helical wake vortex is observed, comprising both tip and root vortices. Over the wave period, the platform's periodic motion modulates the trajectory of the tip vortices, transforming the initially helical wake into a more complex spiral loop wake pattern.

To investigate the influence of platform motions on wake vortex dynamics, we analyze the spatial distance between the leading-edge vortex filaments L_1 (near the rotor plane) and a representative vortex filament within the wake region L_2 (see Fig. 16). Taking Platform 1 in Case 1 as an example (see Fig. 16), comparing time t and $t + T/4$, the spacing between L_1 and L_2 increases. In contrast, comparing the instants at t+2T/4 and t+3T/4, the vortex spacing decreases. This behavior is due to the platform undergoing a decreasing surge around $t \sim t + T/4$ (moving upstream, see Fig. 15(a)). This alters the relative position between the rotor and the shed blade-tip vortices, effectively moving the rotor away from its own wake. This causes the wake to stretch, increasing the spacing between adjacent vortex filaments. Conversely, between t+2T/4 and t+3T/4, as the platform moves downstream (see Fig. 15(a)), the rotor blades momentarily move into their own wake flow. In this condition, they partially "catch up" with the vortex filaments shed previously, compressing the vortex tubes in the downstream direction and reducing the distance between neighboring vortex tubes. Consequently, the wake flow becomes denser and the vortex filaments are more closely packed. Therefore, the spiral wake alternates between stretched and compressed loops throughout the surge period. This phenomenon is consistent with observations reported by Fang et al. (2021).

In addition to surge-induced variations, platform's pitch oscillation introduces significant asymmetry in the vortex shedding pattern along the vertical direction of the rotor. Compared time instant t to $t + T/4$, as the platform pitches forward (i.e., the nacelle tilts down, see Fig. 15(b)), the rotor disk inclines into the incoming wind. This changes the local angle of attack, particularly affecting the distribution of aerodynamic loading along the blade span. As a result, the upper-tip vortices are stretched downstream, while the lower vortices are slightly compressed, leading to an asymmetry in vortex spacing between the upper and lower parts of the wake. Conversely, compared the interval from $t + T/4$ to t+3T/4, the platform pitches backward (i.e., the nacelle tilts upward, see Fig. 15(b)). This motion causes the upper vortices to compress and the lower vortices to stretch, resulting in a reduction in axial spacing between reference vortices L_1 and L_2. This asymmetric vortex deformation demonstrates the dynamic influence of platform pitch on wake coherence and spacing, which has important implications for wake interaction

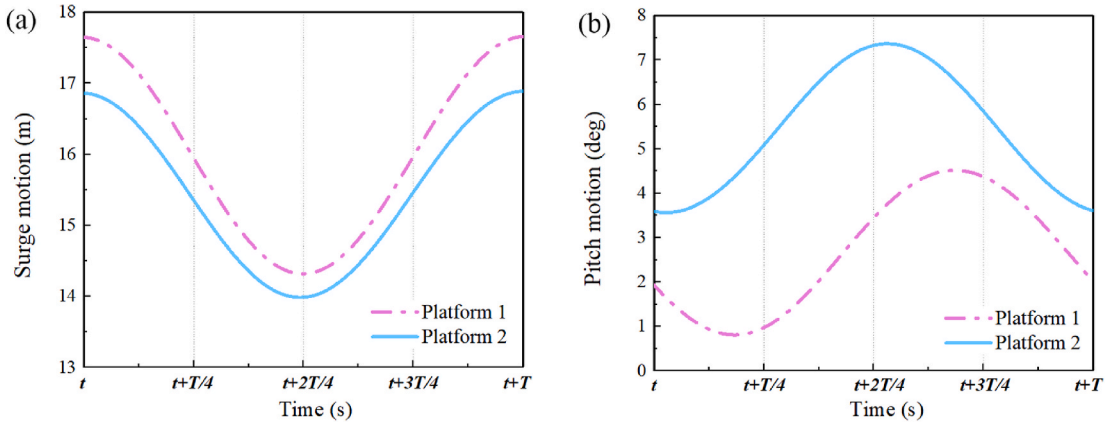

Fig. 15. Surge and pitch motion analysis across one wave period.

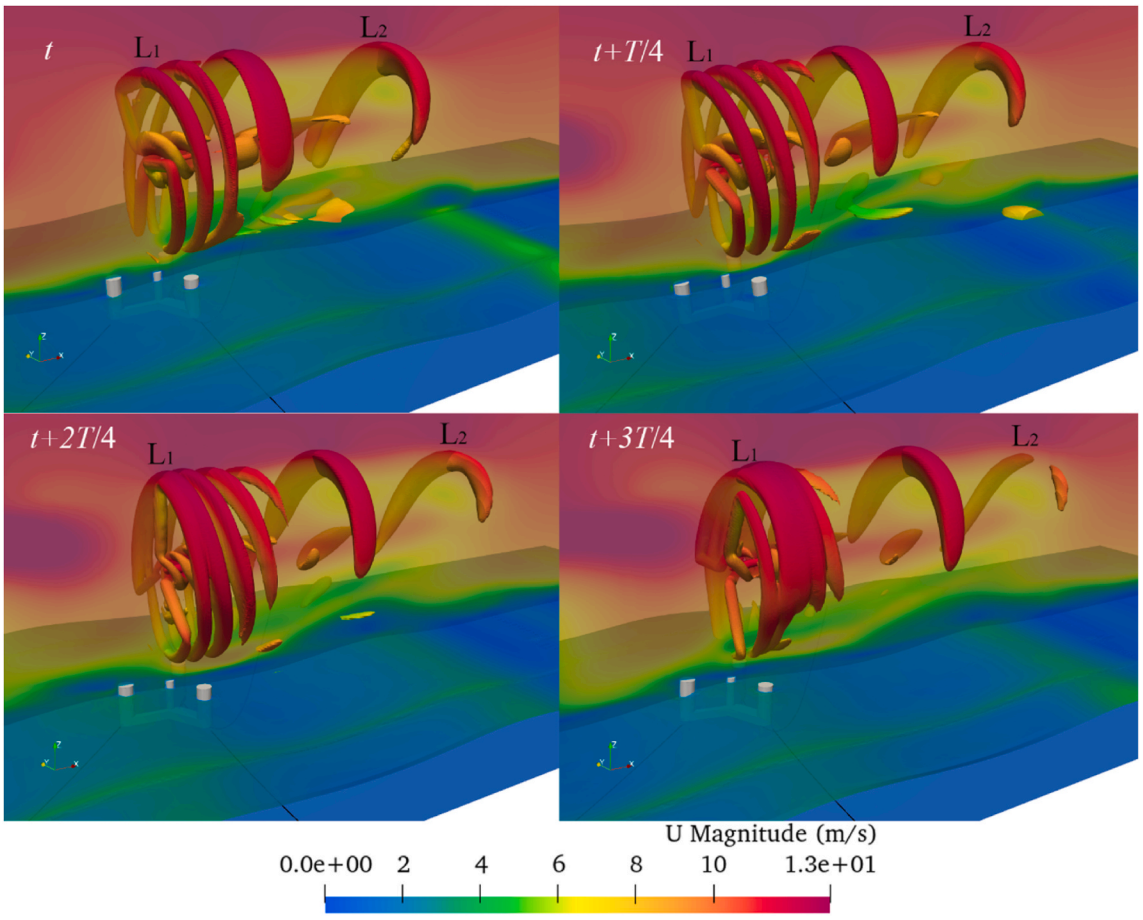

Fig. 16. Visualization of wake vortex of the Platform 1 across one wave period.

and downstream turbine performance in floating wind farms.

These variations in vortex tube spacing are significant because they affect the wake's stability and recovery: denser wake regions exhibit stronger vortex interactions, potentially enhancing turbulence and accelerating wake breakdown, while more stretched wakes may be more stable but exhibit slower energy recovery downstream. Thus, the platform's motion-induced unsteadiness can lead to fluctuating wake characteristics, impacting the performance and fatigue loading of downstream turbines.

Compared to Platform 1, Platform 2 exhibits highly variable and larger vortex tube spacing (see Fig. 17). This can be attributed to the larger pitch motions of Platform 2, which cause the vortex tubes to interact more strongly. This increased interaction may lead to the merging or splitting of vortex tubes, further increasing the variability in spacing.

In summary, the rotor–wake interaction is strongly influenced by the surge and pitch motions of the floating platform. Moreover, different platform configurations exhibit distinct motion responses, resulting in varying impacts on the near-wake structure. These motions dynamically modulate the blade aerodynamics, leading to time-varying blade-tip vortex shedding and wake deformation. Such effects have important implications for wake stability, energy production efficiency, and the optimal design of floating wind turbine arrays.

4.4. Mooring dynamics

The mooring system of a floating offshore wind turbine plays a crucial role in maintaining the stability of the turbine, limiting the platform's motion response, ensuring normal turbine operation, and optimizing power generation efficiency. Therefore, studying the dynamic response of the mooring system is essential. The dynamic response curves of the mooring line tensions for both platforms in both load cases are shown in Fig. 18. The tension in Mooring Line 1 is consistently greater than that in Mooring Line 2 due to its alignment with wind and wave direction. For Mooring Line 1, the fluctuating mooring tension amplitude of Platform 1 are larger than that of Platform 2 for both load cases. In Case 1, the peak tension in Mooring Line 1 is 1.79 MN for Platform 1, while for Platform 2, the tension is slightly reduced by 7.82 %, reaching 1.65 MN. In Case 2, the peak tension in Mooring Line 1 is 1.58 MN for Platform 1, while for Platform 2, it is slightly lower at 1.54 MN, representing a 2.85 % reduction. In contrast, for Mooring Line 2, both the peak tension and the fluctuating tension amplitude of Platform 2 are greater than those of Platform 1. In Case 1, the peak tension in Mooring Line 2 for Platform 2 is 0.60 MN, which is 3.33 % higher than the corresponding peak tension of 0.58 MN observed in Platform 1. In Case 2, the peak tension for Platform 2 is 0.60 MN, representing a 1.67 % increase compared to the 0.59 MN observed in Platform 1.

In Platform 2, the smaller column diameter and increased spacing between the offset columns result in a more evenly distributed hydrodynamic load across the platform. This configuration enhances the platform's wave resistance, leading to lower tension in Mooring Line 1 compared to Platform 1. Additionally, the increased spacing between the offset columns shifts the hydrodynamic center further aft, causing greater platform drift and amplified drag forces on the leeward-side mooring lines. In contrast, Platform 1, exhibits a reduced drift effect and smaller forces on the leeward-side mooring lines. This difference underscores the influence of platform geometry on the dynamic response of the mooring system.

The response spectra of the mooring line tensions for both platforms

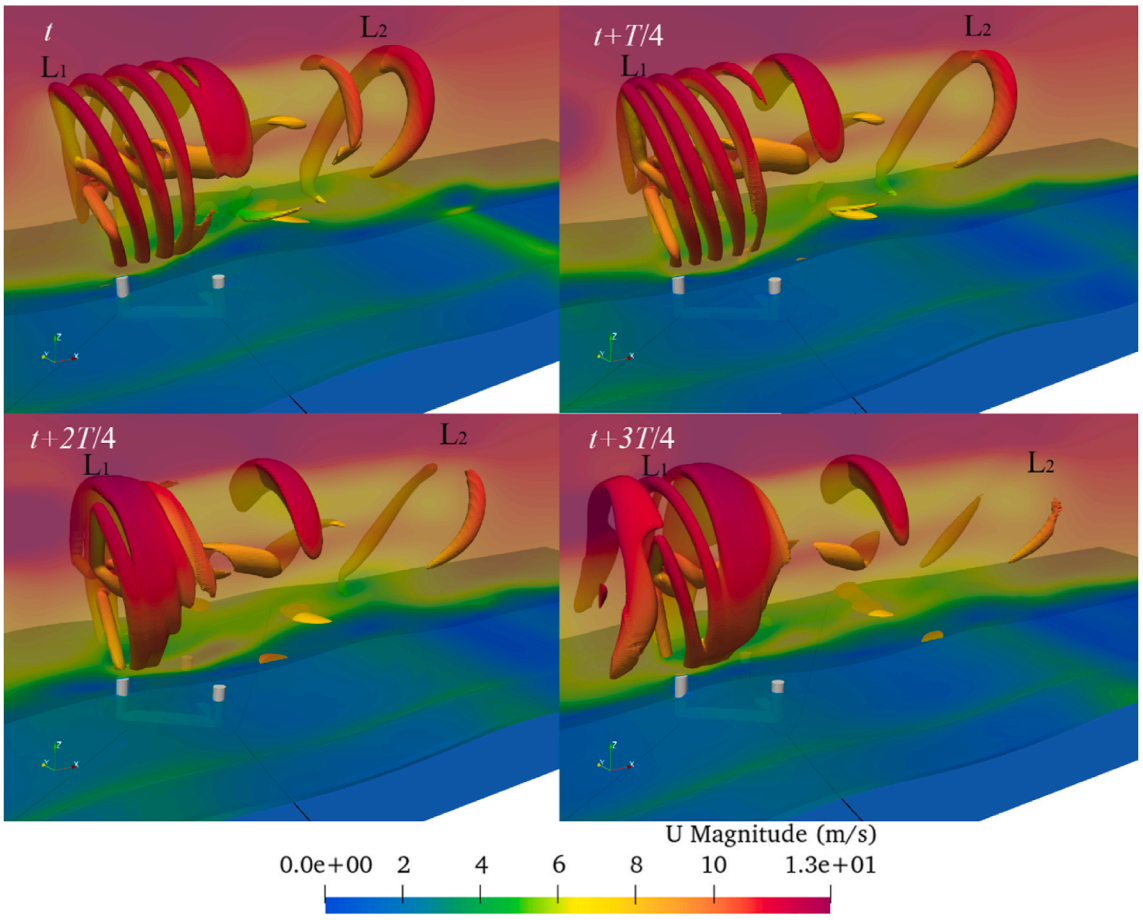

Fig. 17. Visualization of wake vortex of the Platform 2 across one wave period.

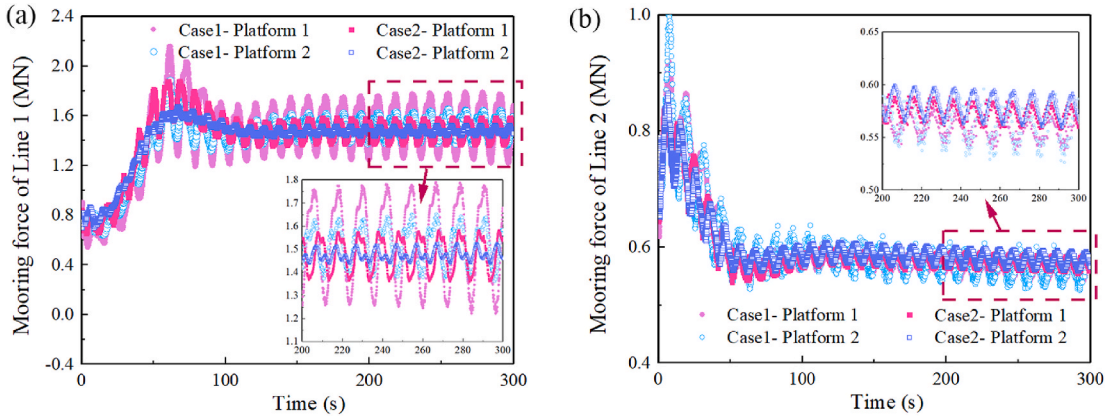

Fig. 18. Mooring dynamics of the two platforms in time-domain. (a) line 1; (b) line 2.

are presented in Fig. 19. The spectral trends for Platform 1 and Platform 2 exhibit similar characteristics, with prominent peak frequencies observed at 0.003 Hz and 0.009 Hz, corresponding to the surge natural frequencies. Additionally, peaks at 0.083 Hz (for Case 1) and 0.1 Hz (for Case 2) and their higher harmonics, corresponding to wave frequencies, are also evident. The presence of higher-order wave frequency peaks is primarily attributable to the combined effects of wave nonlinearity, the coupled dynamics of the floating body and mooring system, and the inherent nonlinearities within the system. The interaction between the floating body, mooring chain, and waves gives rise to a highly coupled dynamic system, where nonlinear wave forces are transmitted through the coupled response of the multi-body system. These forces are then transferred to the mooring chain, amplifying the higher-order frequency components. Consequently, the tension in the mooring lines is predominantly governed by both the surge frequency and wave frequencies. These findings offer valuable insights for the future design and optimization of mooring systems in floating offshore wind turbines.

5. Economic analysis

Although both platform types demonstrate distinct advantages in terms of hydrodynamic performance, the design objectives for floating

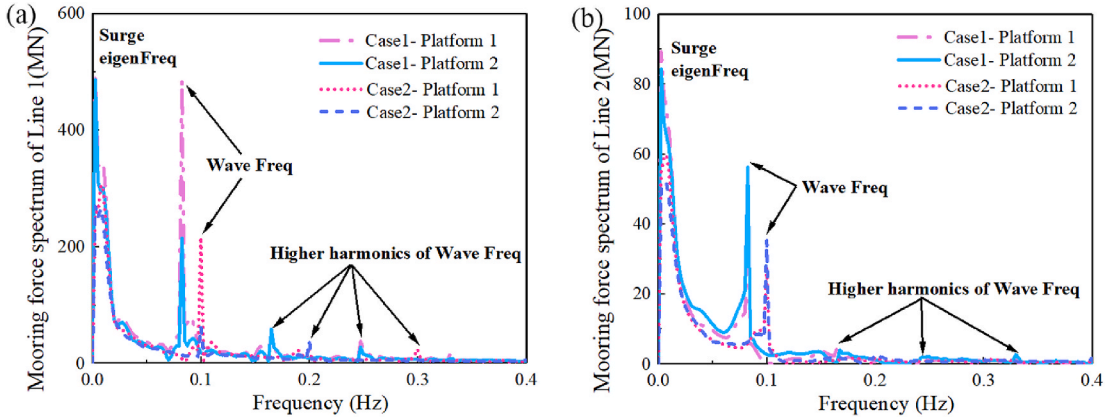

Fig. 19. Mooring dynamics of the two platforms in frequency-domain. (a) line 1; (b) line 2.

wind turbine platforms extend beyond achieving favorable motion responses. A critical factor in platform design is the optimization of economic efficiency, which entails minimizing both initial capital investment and ongoing operational costs, while simultaneously meeting performance and stability requirements. Therefore, a comprehensive economic analysis of these two platform configurations is essential for guiding informed decision-making in platform design and selection. In static equilibrium, the hydrostatic behavior of floating wind turbines in pitch can be described by the buoyancy equation and the restoring equation, as expressed in Eqs.22 and 23

$$F_b = mg \tag{22}$$

$$(\rho g I + F_b z_{CB} - F_w z_{CG})\sin\theta = F_t(h_{hub} + f_b + z_{CB}) - M_m \tag{23}$$

where I is the second moment of inertia of the waterplane area; z_{CB} is the center of buoyancy, z_{CG} is the center of gravity; F_t is the thrust force, θ is the inclination angle, h_{hub} is the hub height; f_b is free board height; V is the volume of the displaced fluid; g is the gravity acceleration; ρ is the fluid density; M_m is the external moment from mooring lines. The mooring lines primarily provide restoring forces in the surge, sway, and yaw degrees of freedom. Since this study focuses primarily on the pitch degree of freedom, the stiffness contributions from the mooring lines are omitted for simplicity and to streamline the analysis.

The vertical center of gravity of the FOWT, consisting of the rotor-nacelle assembly, tower, and hull, can be calculated by summing the individual components' masses, as described in Eq. (24).

$$z_{CG} = \frac{\sum w_i z_{CGi}}{\sum w_i} \tag{24}$$

where w_i is the weight of the ith structure component. z_{CGi} is the center of gravity of the ith component.

The vertical center of buoyancy, defined by the center of mass for the volume of the displaced fluid, is given by Eq. (25)

$$z_{CB} = \frac{\sum V_i z_{CBi}}{V_{disp}} \tag{25}$$

where V_{disp} is the total displaced fluid volume; V_i is the displaced fluid volume of the ith component; z_{CBi} is the vertical center of buoyancy of the ith component.

To calculate the second moment of inertia of the waterplane area I, the parallel axis theorem is applied. For a semi-submerisible platform with circular columns, it can be calucated as Eq. (26)

$$I = nA_0\left(\frac{dc^2}{2} + \frac{A_0}{4\pi}\right) + \frac{A_C^2}{4\pi} \tag{26}$$

where d_c is the radial distance of the columns respect the center of wind turbine. A_0 and A_c are the cross-section area of the offset and central circular columns, respectively. n is the number of offset circular columns.

The concrete substructure is considered one of the most cost-effective materials for floating platforms, owing to its high robustness, extended service life, and low maintenance requirements. The shipyard industry, which is well-established and efficient, further supports the feasibility of concrete-based platforms. Given its advantageous properties, concrete presents a substantial opportunity for cost reduction. As such, this study explores the economic implications of using a concrete-based substructure. For this analysis, a concrete substructure with a thickness of 0.3 m and a density of 2400 kg/m^3 is assumed. The cost of concrete is taken as 77 £/tonne (Ioannou et al., 2020).

The rated thrust of the NREL's 5 MW wind turbine is 823.2 kN (Zhao et al., 2014). The inclination angle, θ, is assumed to be 5° based on the hydrostatic laws governing pitch restoration (Ioannou et al., 2020). The center of gravity of the wind turbine is located at half the hub height ($z_{CG,\ turbine} = h_{hub}/2$). The central column diameter is set equal to the tower base diameter, which is 6.5 m, and the freeboard is 10 m for both platform types. Additionally, seawater ballast, with a density of 1025 kg/m^3, is assumed to fill 70 % of the pontoon volume.

Fig. 20 shows the draft d, radius of the columns R, and the distance between the center of columns and the wind turbine d_c. To satisfy the hydrostatic analysis given by Eqs.22 and 23, the value of column radius R and the distance d_c can be calculated for a given draft d.

Fig. 21(a) illustrates the relationship between d, R, and d_c for the two platform types. It is evident that, with an increase in draft depth d, the offset column radius R tends to decrease, while the central column diameter d_c shows an increasing trend. A comparison of the two platform types reveals that, for the same values of R or d_c, the draft depth d of Platform 2 is smaller than that of Platform 1. Conversely, for a given draft depth d, Platform 2 generally requires a smaller offset column diameter R and a larger spacing between the offset columns. The reduction in R decreases the wave loading area on individual columns, thus reducing the overall wave-induced forces on the platform and enhancing its wave resistance. However, a wider spacing between the offset columns increases the span of the pontoons and deck structures, which may result in higher bending moments and shear forces on these components. This design trade-off underscores the balance between optimizing hydrodynamic performance and maintaining structural integrity.

Fig. 21(b) compares the material costs of the two platform types. Notably, for Platform 1, the material cost exhibits a minimum at a critical draft depth d. As d increases, the total column height increases, driving up material costs. However, the reduction in R with increasing d offsets some of this cost, leading to a critical draft depth where material costs are minimized. In contrast, the material cost for Platform 2 increases approximately linearly with d. For the same draft depth and

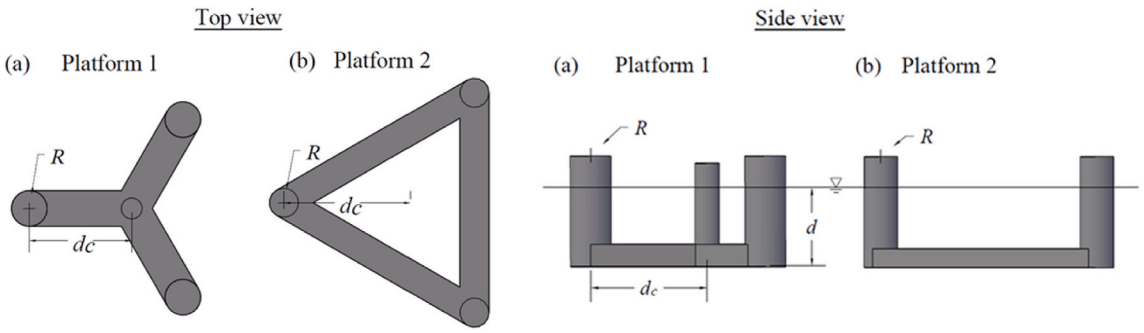

Fig. 20. Parameters of the platform. (a) Top view; (b) side view.

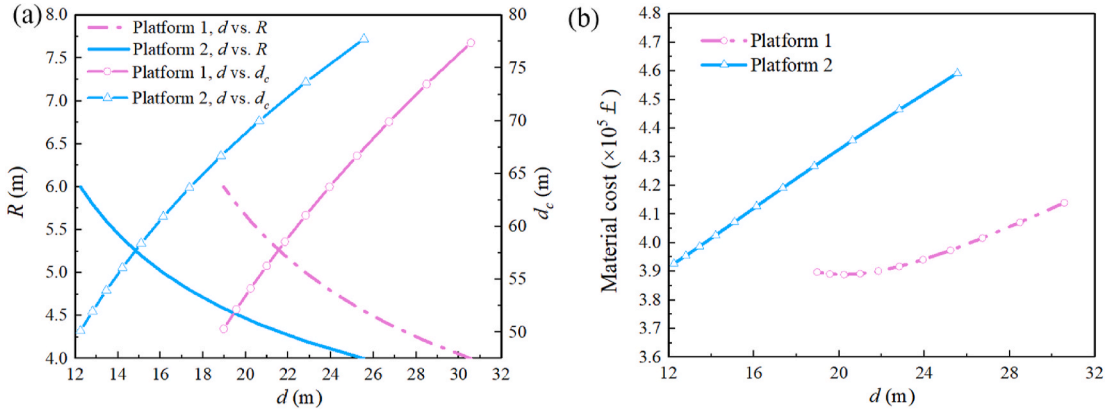

Fig. 21. Parametric analysis of the two platforms. (a) Geometric dimensions; (b) material cost.

ballast water ratio, Platform 2 incurs higher material costs compared to Platform 1. Additionally, at the same draft depth, Platform 2 requires more ballast water, further impacting its overall cost efficiency.

6. Discussion

The three-column semi-submersible platform, characterized by its simpler geometry and fewer components, is often favored for its ease of manufacturing. Its compact and lightweight structure makes it an attractive option for moderate sea conditions and medium-sized wind turbines. However, the three-column design faces challenges under extreme wave and wind conditions. Specifically, the platform tends to exhibit larger tilt amplitudes under wind and wave loading, particularly in roll and pitch motions. This could negatively impact the performance and safety of the wind turbine, particularly in harsher environmental conditions. For deep-draft, large-scale wind turbines, the three-column platform often requires increased column spacing to achieve sufficient waterplane area moment of inertia, thereby improving the restoring moment. This design choice leads to increased material costs due to the need for longer pontoons and larger structural dimensions. In addition, for a three-column semi-submersible FOWT, the turbine tower is typically mounted on one of the outer columns, resulting in an asymmetric mass distribution. Therefore, ballast water adjustment is essential to maintain hydrostatic equilibrium and platform stability. Dynamic ballast control may also be employed to respond to time-varying loads or to assist in active motion damping.

In contrast, the three-column platform with a central column offers enhanced stability, owing to its higher buoyancy and more evenly distributed center of gravity. This configuration demonstrates superior resistance to large waves and wind loads, making it particularly advantageous for large-scale wind turbines, where minimizing platform motion is critical to maintaining turbine efficiency. The inclusion of a central column, however, exposes it directly to wave action, resulting in higher wave excitation forces acting on the platform. Furthermore, the center column introduces more complex construction and installation procedures, such as increased splicing and lifting operations, which can lead to higher labor costs and longer construction timelines. The joint between the center column and pontoons also experiences more complex loading conditions, requiring careful structural design. For deep-draft, however, the material cost of the three-column platform with a central column becomes more cost-effective compared to the standard three-column design.

In conclusion, the choice between the three-column and three-column with central column platforms hinges on balancing simplicity and stability, particularly in challenging marine environments. While the three-column design is well-suited for moderate sea conditions and medium-sized turbines, it faces limitations in extreme conditions. On the other hand, the three-column with central column design offers improved performance and stability for large turbines but at the expense of increased construction complexity.

7. Conclusions

This study provides a comprehensive comparison of two widely adopted semi-submersible floating wind turbine platform configurations: the three-column and the three-column with central column designs. Through advanced numerical simulations integrating fluid-structure interaction and mooring dynamics, the performance of both platforms was assessed under realistic marine conditions. The findings underscore the importance of platform geometry in determining dynamic stability and the efficiency of the mooring system, with significant implications for platform design and installation. The coupling of high-fidelity CFD, the lumped-mass mooring model, and the Actuator Line Model provides a robust framework for understanding the complex interactions between the wind turbine, floating platform, and mooring system. The study also presents an economic analysis, offering valuable

insights into the cost-effectiveness of the two platform types. Future research should focus on optimizing these designs by considering varying environmental conditions and advancing simulation techniques to improve the prediction of platform dynamics and enhance the economic feasibility of large-scale floating wind turbine installations. The main findings are summarized as follows:

(1) The results demonstrate that platform geometry critically influences motion stability. While the three-column platform shows superior surge stability, the introduction of a central column significantly enhances pitch and heave stability—particularly under combined wind and wave conditions—leading to a 38.7 % reduction in maximum pitch angle.
(2) Floating platform motion strongly modulates wake behavior. Specifically, pitch motion induces asymmetric deformation of vortex filaments. The spiral wake alternates between stretched and compressed loops throughout the platform surge period.
(3) The wake structure and rotor aerodynamics were found to be highly sensitive to platform configuration. The central column design alters the periodic motion characteristics, influencing vortex shedding and wake expansion. These interactions affect instantaneous rotor loading and could guide control strategies for mitigating unsteady aerodynamic loads.
(4) Significant differences in mooring line dynamics were observed between the two configurations. The central-column platform, particularly with upstream-aligned mooring lines, exhibited more complex fairlead motions and higher peak line tensions.
(5) From a techno-economic perspective, the addition of a central column can improve dynamic performance without proportionally increasing material cost. For deep-draft and large-scale applications, the modified design potentially offers a more cost-effective balance between stability and construction feasibility compared to the standard three-column design.

The findings of this study aim to enhance the design, performance, and cost-effectiveness of floating wind turbine platforms, supporting their development for commercial-scale offshore winds. Future studies could expand the environmental scenarios, including irregular waves and extreme weather conditions such as typhoons and cyclones, to further evaluate the different types of platforms' resilience and performance in a wider range of sea states.

CRediT authorship contribution statement

Pengxu Zou: Writing – original draft, Visualization, Validation, Software, Methodology, Formal analysis, Conceptualization. **Jeremy D. Bricker:** Writing – review & editing, Supervision.

Declaration of competing interest

The authors declare that they have no known competing financial interests or personal relationships that could have appeared to influence the work reported in this paper.

Acknowledgement

The study presented in this paper was conducted in the floating offshore wind turbine research funded by China Communications Construction Company Ltd. (CCCC). The authors also acknowledge a 2023 catalyst grant from the Michigan Institute for Computational Discovery and Engineering (MICDE).

Nomenclature

Acronym	
ALM	Actuator Line Model
BEM	Blade Element Momentum
CFD	Computational Fluid Dynamics
DoFs	Degrees of Freedom
FFT	Fast Fourier Transform
FOWT	Floating Offshore Wind Turbine
FSI	Fluid-Structure Interaction
GM	Metacentric Height
ODE	Ordinary Differential Equation
RANS	Reynolds-Averaged Navier-Stokes
SST	Shear Stress Transport
SWL	Still Water Level
TLP	Tension Leg Platform
TSR	Tip-Speed Ratio
VOF	Volume of Fluid
Symbol	
A_0	Cross-section area of the offset circular columns
A_c	Cross-section area of the central circular columns
A_i	Oscillation amplitude at the ith period
C	Axial structural damping
C_d	Drag coefficient
C_l	Lift coefficient
d_c	Radial distance of the columns respect the center of wind turbine
E	Young's elastic modulus
f	External force
f_b	Free board height
$\mathbf{F}_i$	Tensor for the point forces
F_t	Thrust force
g	Gravity acceleration
h_{hub}	Hub height
I	Second moment of inertia of the waterplane area
$\mathbf{J}$	Time-invariant inertia matrix relative to the center of mass
k	Turbulence kinetic energy
m	Total mass

(*continued on next page*)

(*continued*)

M_m	External moment from mooring lines
n	Number of offset circular columns.
p	Pressure
$\mathbf{S}$	Surface of the boundary patch for the rigid floating body
t	Time
T	Axial stiffness
U_0	Inflow velocity vector
U_p	Airfoil velocity term
U_r	Component of the inflow velocity in the rotor plane
U_{rel}	Total relative velocity
v	Velocity
V	Volume of the displaced fluid
V_{disp}	Total displaced fluid volume
w_i	Weight of the ith structure component
z_0	Surface roughness length
Z_{CB}	Center of buoyancy
z_{CBi}	Vertical center of buoyancy of the ith component
Z_{CG}	Center of gravity
z_{CGi}	Center of gravity of the ith component
ε	Segment strain
ζ	Damping ratio
θ	Inclination angle
μ	Dynamic viscosity
ρ	Fluid density
σ	Volume fraction
ω	Turbulence specific dissipation rate

References

Adnan Durakovic, "WindFloat Atlantic." Accessed: September. 2, 2025. [Online]. Available: https://www.offshorewind.biz/%0A2020/07/27/windfloat-atlantic-fully-up-and-running/.

Alkhabbaz, A., et al., 2024. The aero-hydrodynamic interference impact on the NREL 5-MW floating wind turbine experiencing surge motion. Ocean Eng. 295, 116970.

Bachant, P., Goude, A., daa-mec, Wosnik, M., Adhyanth, Delicious, M.G., 2025. turbinesFoam/turbinesFoam: V0.2.1. Zenodo. https://doi.org/10.5281/zenodo.14640307.

Cai, Y., Li, X., Zhao, H., Shi, W., Wang, Z., 2025. Developing a multi-region coupled analysis method for floating offshore wind turbine based on OpenFOAM. Renew. Energy 238, 122026.

Cheng, P., Huang, Y., Wan, D., 2019. A numerical model for fully coupled aero-hydrodynamic analysis of floating offshore wind turbine. Ocean Eng. 173, 183–196. https://doi.org/10.1016/j.oceaneng.2018.12.021.

Clement, C., Kosleck, S., Lie, T., 2021. Investigation of viscous damping effect on the coupled dynamic response of a hybrid floating platform concept for offshore wind turbines. Ocean Eng. 225. https://doi.org/10.1016/j.oceaneng.2021.108836.

CSSC, "'Fu Yao' rises into the sky, chasing the deep sea." [Online]. Available: http://cssc-hz.com/?en/enNews/NewsReleases/121.html.

Ding, Q., Li, C., Yu, N., Hao, W., Ji, J., 2018. Numerical and experimental investigation into the dynamic response of a floating wind turbine spar array platform. J. Mech. Sci. Technol. 32 (3), 1106–1116. https://doi.org/10.1007/s12206-018-0213-x.

Dunbar, A.J., Craven, B.A., Paterson, E.G., 2015. Development and validation of a tightly coupled CFD/6-DOF solver for simulating floating offshore wind turbine platforms. Ocean Eng. 110, 98–105. https://doi.org/10.1016/j.oceaneng.2015.08.066.

Fang, Y., Li, G., Duan, L., Han, Z., Zhao, Y., 2021. Effect of surge motion on rotor aerodynamics and wake characteristics of a floating horizontal-axis wind turbine. Energy (Calg.) 218, 119519.

Franke, J., et al., 2004. Recommendations on the use of CFD in wind engineering. In: COST Action C14: Impact of Wind and Storm on City Life and Urban Environment.

Goupee, A.J., Koo, B.J., Kimball, R.W., Lambrakos, K.F., Dagher, H.J., 2014. Experimental comparison of three floating wind turbine concepts. J. Offshore Mech. Arctic Eng. 136 (2). https://doi.org/10.1115/1.4025804.

Haider, R., Shi, W., Cai, Y., Lin, Z., Li, X., Hu, Z., 2024. A comprehensive numerical model for aero-hydro-mooring analysis of a floating offshore wind turbine. Renew. Energy 237, 121793.

Hall, M., 2020. Moordyn v2: new capabilities in mooring system components and load cases. In: Proceedings of the International Conference on Offshore Mechanics and Arctic Engineering - OMAE. https://doi.org/10.1115/omae2020-19341.

Hirt, C.W., Nichols, B.D., 1981. Volume of fluid (VOF) method for the dynamics of free boundaries. J. Comput. Phys. https://doi.org/10.1016/0021-9991(81)90145-5.

Ioannou, A., Liang, Y., Jalón, M.L., Brennan, F.P., 2020. A preliminary parametric techno-economic study of offshore wind floater concepts. Ocean Eng. 197. https://doi.org/10.1016/j.oceaneng.2020.106937.

Jacobsen, N.G., Fuhrman, D.R., Fredsøe, J., 2012. A wave generation toolbox for the open-source CFD library: OpenFoam®. Int. J. Numer. Methods Fluid. 70 (9). https://doi.org/10.1002/fld.2726.

Jonkman, J.M., Matha, D., 2011. Dynamics of offshore floating wind turbines-analysis of three concepts. Wind Energy 14 (4). https://doi.org/10.1002/we.442.

Jonkman, J., Butterfield, S., Musial, W., Scott, G., 2009. Definition of a 5-MW reference wind turbine for offshore system development. Contract 1–75. February [Online]. Available: http://tethys-development.pnnl.gov/sites/default/files/publications/Jonkman_et_al_2009.pdf.

Karimirad, M., Moan, T., 2012. A simplified method for coupled analysis of floating offshore wind turbines. Mar. Struct. 27 (1), 45–63. https://doi.org/10.1016/j.marstruc.2012.03.003.

Leble, V., Barakos, G., 2016. Demonstration of a coupled floating offshore wind turbine analysis with high-fidelity methods. J. Fluid Struct. 62, 272–293. https://doi.org/10.1016/j.jfluidstructs.2016.02.001.

Li, C., et al., 2022. Dynamics of a Y-shaped semi-submersible floating wind turbine: a comparison of concrete and steel support structures. Ships Offshore Struct. 17 (8). https://doi.org/10.1080/17445302.2021.1937801.

Lin, X.F., Zhang, J.S., Zhang, Y.Q., Zhang, J., Liu, S., 2019. Comparison of actuator line method and full rotor geometry simulations of the wake field of a tidal stream turbine. Water (Switzerland) 11 (3). https://doi.org/10.3390/w11030560.

Liu, Y., Xiao, Q., Incecik, A., Peyrard, C., Wan, D., 2017. Establishing a fully coupled CFD analysis tool for floating offshore wind turbines. Renew. Energy 112, 280–301. https://doi.org/10.1016/j.renene.2017.04.052.

Matha, D., 2010. Model development and loads analysis of an offshore wind turbine on a tension leg platform, with a comparison to other floating turbine concepts: April 2009 (No. NREL/SR-500-45891). National Renewable Energy Lab.(NREL).

Nygaard, T.A., De Vaal, J., Pierella, F., Oggiano, L., Stenbro, R., 2016. Development, verification and validation of 3DFloat; aero-servo-hydro-elastic computations of offshore structures. In: Energy Procedia, pp. 425–433. https://doi.org/10.1016/j.egypro.2016.09.210.

Ohta, M., Komatsu, M., Ito, H., Kumamoto, H., 2013. Development of a V-shaped semi-submersible floating structure for 7MW offshore wind turbine. Proc. Int. Symp. Mar. Offshore Renew. Energy. Tokyo, Japan, 28–30.

olavolsen, 2011. OO-Star wind floater development [Online]. Available: https://www.olavolsen.no/en/departments/renewable-energy.

Onel, H.C., Tuncer, I.H., 2021. Investigation of wind turbine wakes and wake recovery in a tandem configuration using actuator line model with LES. Comput. Fluids 220. https://doi.org/10.1016/j.compfluid.2021.104872.

Pericas, P.F., 2022. CFD Simulation of a Floating Wind Turbine with Openfoam: an FSI Approach Based on the Actuator Line and Relaxation Zone Methods. Delft University of Technology Delft, The Netherlands.

Rai, R.K., Gopalan, H., Sitaraman, J., Mirocha, J.D., Miller, W.O., 2017. A code-independent generalized actuator line model for wind farm aerodynamics over simple and complex terrain. Environ. Model. Software 94, 172–185. https://doi.org/10.1016/j.envsoft.2017.05.001.

Robertson, A., Jonkman, J., Masciola, M., Song, H., Goupee, A., Coulling, A., Luan, C., 2014. *Definition of the semisubmersible floating system for phase II of OC4* (No. NREL/TP-5000-60601). National Renewable Energy Lab.(NREL).

Rocchio, B., Ciri, U., Salvetti, M.V., Leonardi, S., 2020. Appraisal and calibration of the actuator line model for the prediction of turbulent separated wakes. Wind Energy 23 (5), 1231–1248. https://doi.org/10.1002/we.2483.

Saeki, M., Tobinaga, I., Sugino, J., Shiraishi, T., 2014. Development of 5-MW offshore wind turbine and 2-MW floating offshore wind turbine technology. Hitachi Rev. 63 (7).

Sebastian, T., Lackner, M.A., 2013. Characterization of the unsteady aerodynamics of offshore floating wind turbines. Wind Energy 16 (3), 339–352. https://doi.org/10.1002/we.545.

Sørensen, J.N., Shen, W.Z., 2002. Numerical modeling of wind turbine wakes. J. Fluids Eng. Trans. ASME 124 (2), 393–399. https://doi.org/10.1115/1.1471361.

Stevens, R.J.A.M., Martínez-Tossas, L.A., Meneveau, C., 2018. Comparison of wind farm large eddy simulations using actuator disk and actuator line models with wind tunnel experiments. Renew. Energy 116, 470–478. https://doi.org/10.1016/j.renene.2017.08.072.

Thiagarajan, K.P., Dagher, H.J., 2014. A review of floating platform concepts for offshore wind energy generation. J. Offshore Mech. Arctic Eng. 136 (2). https://doi.org/10.1115/1.4026607.

Tran, T.T., Kim, D.H., 2016a. Fully coupled aero-hydrodynamic analysis of a semi-submersible FOWT using a dynamic fluid body interaction approach. Renew. Energy 92, 244–261. https://doi.org/10.1016/j.renene.2016.02.021.

Tran, T.T., Kim, D.H., 2016b. A CFD study into the influence of unsteady aerodynamic interference on wind turbine surge motion. Renew. Energy 90. https://doi.org/10.1016/j.renene.2015.12.013.

Uzunoglu, E., Guedes Soares, C., 2015. Influence of bracings on the hydrodynamic modelling of a semi-submersible offshore wind turbine platform. Renew. Energies Offshore.Taylor Fr. Gr. 755–762.

Yang, H.-S., Tongphong, W., Ali, A., Lee, Y.-H., 2023. Comparison of different fidelity hydrodynamic-aerodynamic coupled simulation code on the 10 MW semi-submersible type floating offshore wind turbine. Ocean Eng. 281, 114736.

Yang, H.-S., Alkhabbaz, A., Tongphong, W., Lee, Y.-H., 2024. Cross-comparison analysis of environmental load components in extreme conditions for pontoon-connected semi-submersible FOWT using CFD and potential-based tools. Ocean Eng. 304, 117248.

Xu Yihe, “Haiyou guanlan.” [Online]. Available: https://www.upstreamonline.com/energy-transition/china-s-first-deep-water-floating-wind-farm-connected-to-the-grid/2-1-1453812.

Young, A.C., Dagher, H.J., Hettick, S., Goupee, A.J., Viselli, A.M., 2014. VolturnUS 1:8-scale FRP floating wind turbine tower: analysis, design, testing and performance. In: Proceedings of the International Conference on Offshore Mechanics and Arctic Engineering - OMAE. https://doi.org/10.1115/OMAE2014-23454.

Zhang, Y., Kim, B., 2018. A fully coupled computational fluid dynamics method for analysis of semi-submersible floating offshorewind turbines underwind-wave excitation conditions based on OC5 data. Appl. Sci. 8 (11). https://doi.org/10.3390/app8112314.

Zhao, W., Cheng, P., Wan, D., 2014. Numerical computation of aerodynamic performances of NREL offshore 5-MW baseline wind turbine. In: Proceedings of the 11th (2014) Pacific/Asia Offshore Mechanics Symposium, PACOMS 2014.

Zhao, Y., Cheng, Z., Gao, Z., Sandvik, P.C., Moan, T., 2019. Numerical study on the feasibility of offshore single blade installation by floating crane vessels. Mar. Struct. 64, 442–462. https://doi.org/10.1016/j.marstruc.2018.12.001.

Zou, P.X., Ruiter, N., Bricker, J.D., Uijttewaal, W.S.J., 2023a. Effects of roughness on hydrodynamic characteristics of a submerged floating tunnel subject to steady currents. Mar. Struct. 89, 103405. https://doi.org/10.1016/j.marstruc.2023.103405.

Zou, P., Kim, T., Bricker, J.D., Uijttewaal, W.S.J., 2023b. Assessment of interfacial turbulence treatment models for free surface flows. J. Hydraul. Res. 61 (5), 651–667.

Zou, P., Bricker, J.D., Fujisaki-Manome, A., Garcia, F.E., 2024. Characteristics of ice-structure-soil interaction of an offshore wind turbine. Ocean Eng. 295, 116975.